Iceberg Drift Ensemble Forecasting

by

© *Evan Kielley*

A thesis submitted to the

School of Graduate Studies

in partial fulfilment of the

requirements for the degree of

Master of *Science* in *Scientific Computing*

Department of *Mathematics and Statistics*

Memorial University of Newfoundland

May 2020

St. John's Newfoundland

Abstract

The goal of this thesis is to investigate whether ensemble modeling in iceberg drift forecasting improves predictions of an iceberg's trajectory. To do this, we have used a dynamic iceberg drift model and created an ensemble of realizations by applying stochastic perturbations to ocean current and wind reanalysis data, drawing from distributions of the ocean current and wind measured with ship-based instruments.

In this study, we focus on simulating trajectories for two icebergs observed during the 2015 Statoil-ArcticNet research expedition. To conduct simulations, we initialized our model with observations of each iceberg at a particular time and location, then simulated a day of drift for each iceberg and compared the ensemble of simulation results to their actual known trajectories. In this comparison, we found inconsistent results. For one iceberg, the mean of the modelled trajectories was consistent with the observations but, for the other, none of the modelled trajectories were close.

Overall, we conclude that ensemble modelling for iceberg drift forecasting is a useful technique only when the wind and current data driving the prediction is sufficiently accurate.

Acknowledgements

First of all, I would like to thank my supervisors, Drs. James Munroe, Scott MacLachlan, and Alex Bihlo, for all their help and guidance. I would also like to thank the School of Graduate Studies for their financial support, the head of the Scientific Computing program, Dr. Ron Haynes, for managing the program, and every member of the administrative staff of the Department of Mathematics and Statistics and the Department of Physics and Physical Oceanography for all their help over the years.

I would also like to thank Dr. Gregory Crocker of the Global Water Institute at Carleton University for laying some of the groundwork upon which this thesis was built and help in acquiring data, Dr. Leopold Haimberger and Michael Mayer of the University of Vienna for their help in acquiring data, Dr. Fraser J.M. Davidson of the Department of Fisheries and Oceans Newfoundland and Labrador for his advice, and Dr. Till Wagner of the University of North Carolina Wilmington for his willingness to help and making his work on iceberg drift available.

Contents

List of Tables

List of Figures

Chapter 1

The Problem

1.1 SeaRose Ice Incursion Incident

At 5:51 AM, on Wednesday 29$^{\text{th}}$ March, 2017, an iceberg passed within 50–100 m of the SeaRose FPSO — a vessel moored in the Grand Banks off the coast of Newfoundland to extract oil from the White Rose oil field (Warren et al., 2018). This incident serves as a grave reminder of the threat that icebergs still pose, some 100 years after the sinking of the Titanic and the creation of the International Ice Patrol (IIP). Why does this problem remain? Largely, it is because the data required to run an iceberg drift model is not measured with enough accuracy to produce an accurate prediction. Therefore, this thesis focuses on determining the current quality of input data and algorithms for predicting iceberg drift and how they might be improved.

Companies that manage vessels that operate in regions where ice poses a risk have emergency procedures that are meant to mitigate the danger of a collision. Referring again to the SeaRose Ice Incursion Incident, the company that manages that vessel,

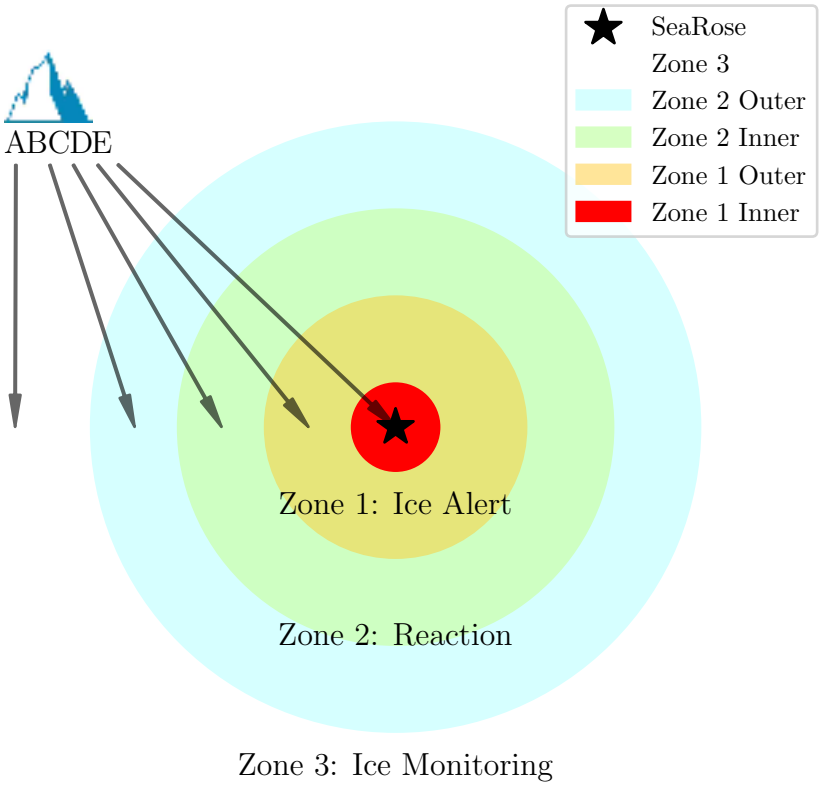

Figure 1.1: Husky's Emergency Management Plan for icebergs. Zone 1, also known as the ice exclusion zone, has a radius of 0.25 nautical miles.

Husky Inc., has an Emergency Management Plan (EMP) that dictates which course of action to take based on how close the forecast trajectory of the iceberg comes to the vessel. A diagram of this plan is shown in Figure 1.1.

In Figure 1.1, the labels A through E represent the different courses of action the company is expected to take. Unfortunately, the current forecast strategy is just to produce a single deterministic iceberg drift track and choose the course of action

that corresponds to that track. The problem with this approach is that there are many uncertainties in the data that drives the iceberg drift model, therefore, such a deterministic track does not represent the inherent variability. For instance, the inner-most circle, the "Ice Exclusion Zone", has a radius of just half a kilometer; therefore, if an iceberg were to drift just a kilometer away from its deterministic path, the response required by Husky could be much different That being said, if we add just a correction to the ocean current velocity by sampling from the current nearby in time and space, we obtain a cone-like trajectory as seen in Figure 1.2.

This technique, known as *ensemble forecasting*, is used extensively in numerical weather prediction, where multiple simulations are created to account for uncertainties that come from errors in the initial conditions and the errors in the model itself and/or the mathematical methods used to solve the equations. For iceberg drift forecasting, these would be the approximate starting location and velocity of the iceberg, the physical iceberg properties (such as the geometry, density, and drag coefficients), the wind and ocean current forecasts, the equations of motion that depict the physics of iceberg drift, and the numerical methods used to solve these equations. In contrast to deterministic forecasting, ensemble forecasting often provides a range of possible outcomes. It is important to note, though, that because the Ice Exclusion Zone is so small, the spread of the ensemble would have to be relatively small too so that the 95% confidence interval of the forecast captures this zone; otherwise, the ensemble forecast would not be as helpful. Therefore, it is the goal of this thesis to explore the benefit that ensemble forecasting could potentially bring to iceberg drift forecasting.

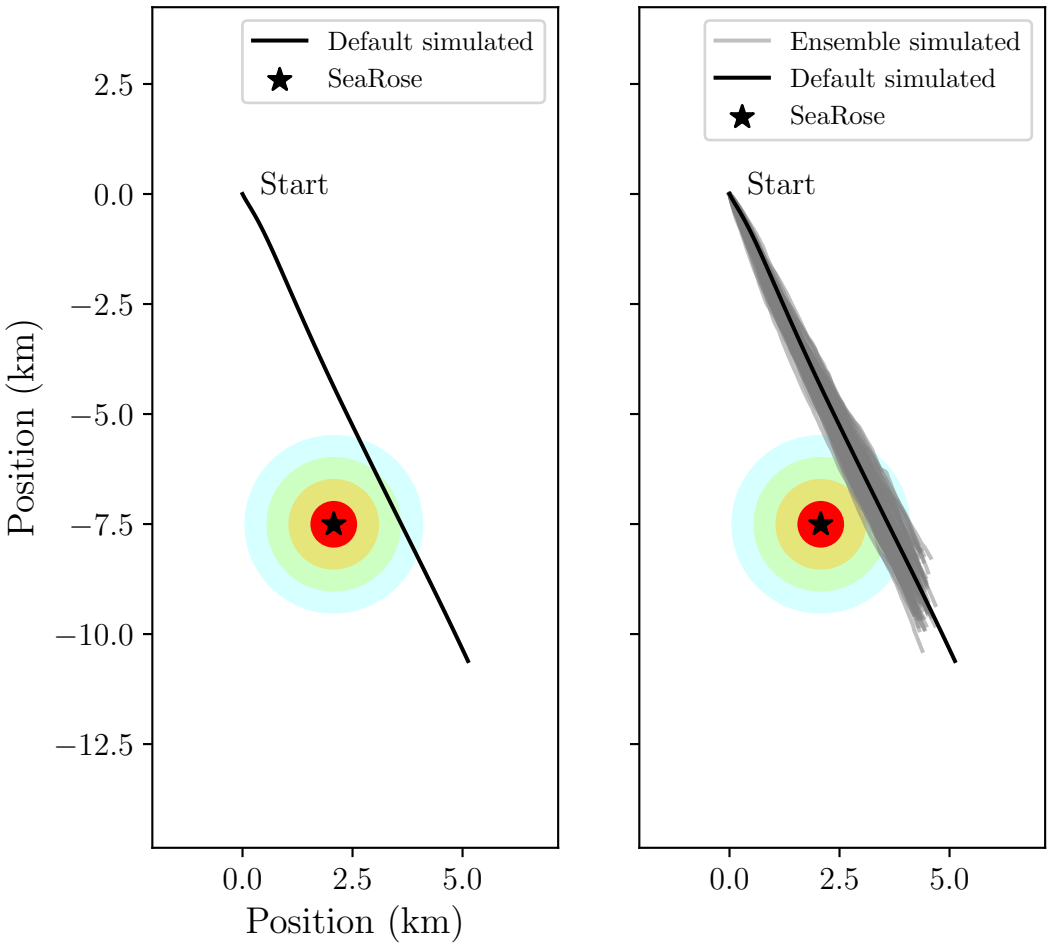

Figure 1.2: Deterministic versus ensemble forecasting in the context of making decisions according to Husky's Emergency Management Plan.

1.2 Summary

Chapter 1 introduces the problem we will be studying. In Chapter 2, we will introduce the fundamentals of the science behind icebergs, winds, and ocean currents and how they relate to the physics of iceberg drift as well as the data for iceberg detection and wind and ocean current forecasts. Then, in Chapter 3, we will cover the physics behind iceberg drift and the iceberg drift models that were used in this project. We also look at various numerical methods used to integrate the equations of motion. After that, in Chapter 4, we will discuss the results of running various drift models with various data sets under different conditions. Namely, we look at two case studies: one that models an iceberg drift prediction well and another that models an iceberg drift prediction poorly. Lastly, in Chapter 5, we will discuss the implications for ensemble iceberg drift forecasting and compare it to different methods that have been previously explored.

Chapter 2

Icebergs, Oceans, and the Atmosphere

2.1 Icebergs

2.1.1 Origin

Icebergs are blocks of ice that have broken away from a glacier (Diemand, 2001). The two regions that are the greatest sources of icebergs are the great ice sheets of Greenland and Antarctica. Since this research focuses on the threat they pose to offshore oil vessels, we will focus on icebergs that originate from Greenland. Most of these icebergs break away from Western Greenland directly into Baffin Bay; however, some come from Eastern Greenland as well. Consequently, some of these icebergs drift out of Baffin Bay, into the Davis Strait, and down the Labrador coast via the cold Labrador Current, eventually making their way into the Grand Banks off Newfoundland, as seen in Figure 2.1.

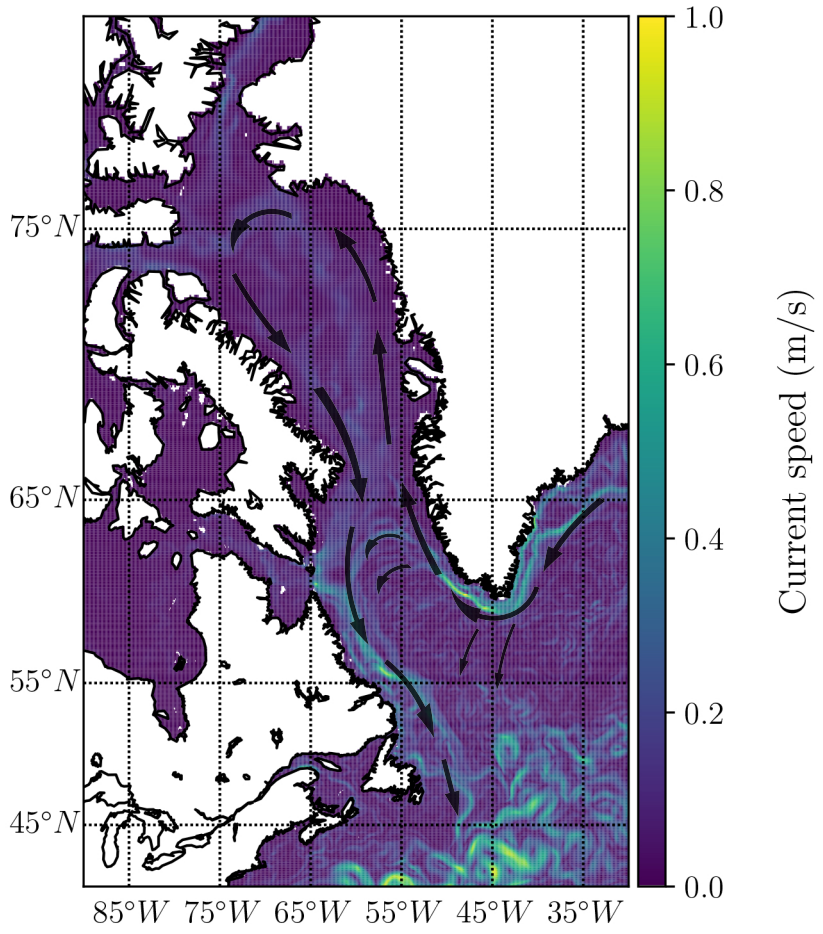

Figure 2.1: Typical positions of icebergs throughout their life cycle.

Information on the size, shape, and location of icebergs adrift in the ocean come from observations made visually and/or by radar from devices on ships or aircraft as well as via satellite imagery. Each of these observational methods, however, has its own strengths and weaknesses. For example, satellite imagery covers very large areas and all times of the year but will not detect small icebergs. A radar, on the other hand, will pick up most icebergs within its range but may miss rounded icebergs or small icebergs in heavy seas. Lastly, observations made visually are good in the sense that they will catch all sizes of icebergs, but only within a limited area in good weather when someone is looking.

The world's largest collector of iceberg sightings is the International Ice Patrol (IIP), an organization formed within the US Coast Guard after the sinking of the Titanic, in 1914. They record information on the sighting of each iceberg that crosses 48° N and store them in the IIP Iceberg Sightings Database, (International Ice Patrol (IIP), 1995, updated 2018). As shown in Figure 2.2, the number of icebergs observed varies significantly from year to year. Figure 2.3 gives an idea of where, geographically speaking, icebergs are observed in a given year.

2.1.2 Physical Properties

Icebergs come in all shapes and sizes but, for illustration purposes, Figure 2.4 shows an iceberg with cuboid geometry just to outline the terminology of its dimensions. However, as icebergs deteriorate, they tend to assume certain characteristic forms (Diemand, 2001). These forms are described by the particular size and shape classes listed in Tables 2.1 and 2.2.

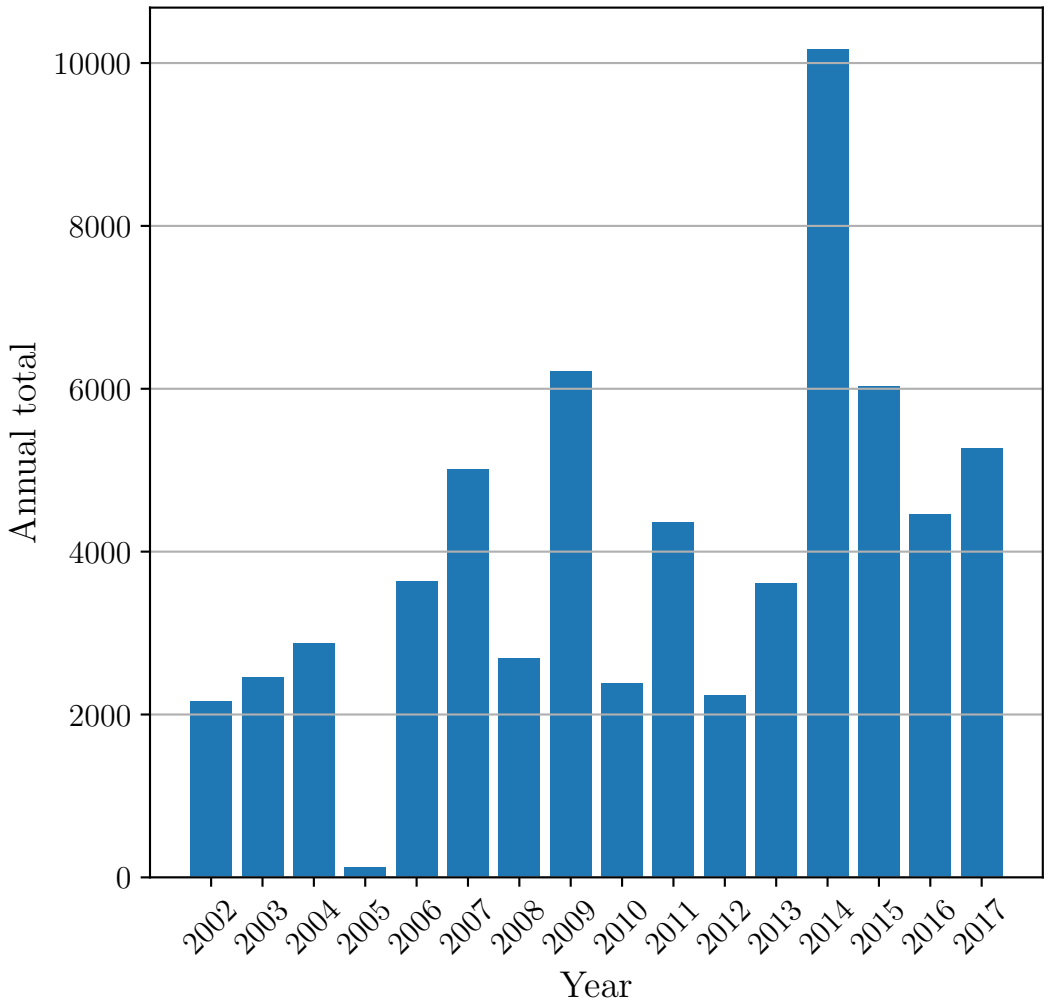

Figure 2.2: Annual total number of unique icebergs observed by the IIP from 2002–2017.

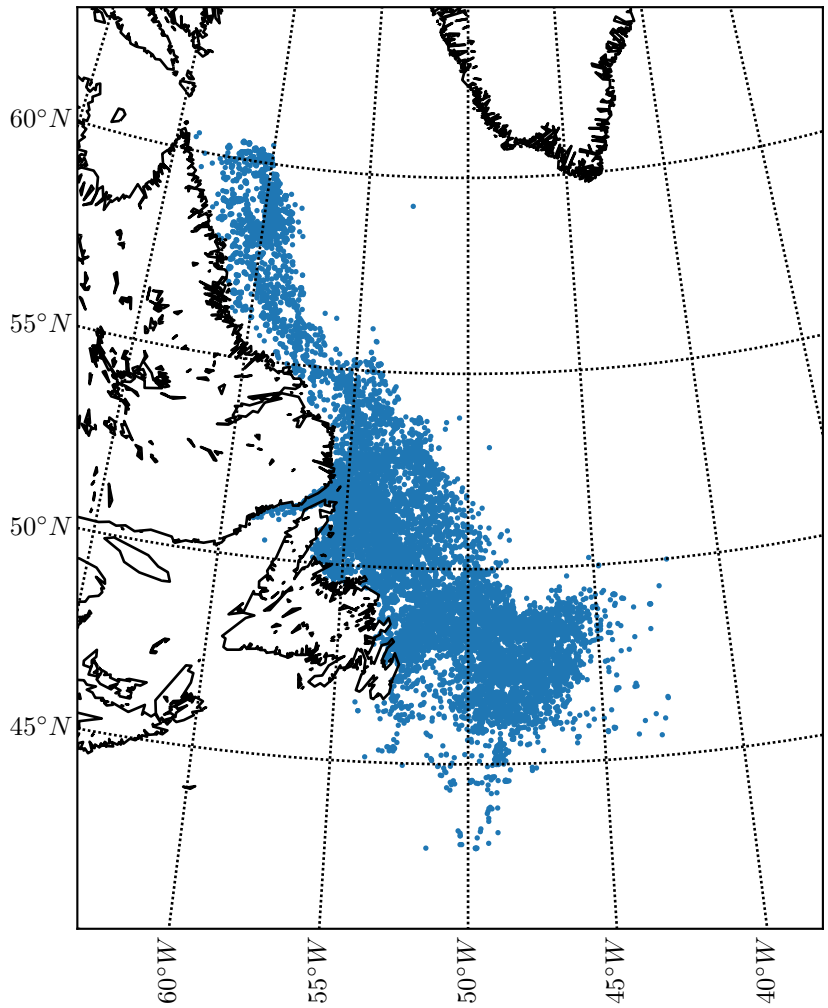

Figure 2.3: Locations of all individual observations made by the IIP in 2015.

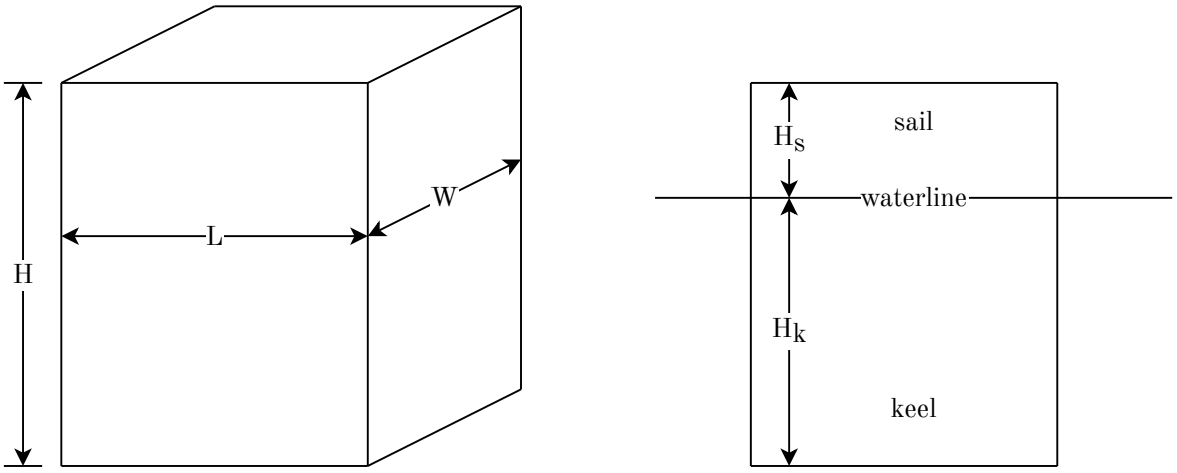

Figure 2.4: Dimensions and cross-sectional area of a cuboid iceberg. In the sub-figure on the left, H, L, and W refer to the height, length, and width of the iceberg; respectively. In the sub-figure on the right, the waterline depicts the surface of the water, the keel is the term used to identify the part of the iceberg below the waterline, the sail is the term used for the part of the iceberg above the waterline, and H_k, H_s are the heights of the keel, sail of the iceberg; respectively.

Size Class	Height (m)	Length (m)
Growler	< 1	< 5
Bergy Bit	1 - 5	5 - 15
Small	5 - 15	15 - 60
Medium	16 - 45	61 - 120
Large	46 - 75	121 - 200
Very Large	> 75	> 200

Table 2.1: Iceberg dimension ranges according to size class (Environment Canada, Meteorological Service of Canada, 2005).

Shape Class	Shape Factor	Height to Draft Ratio
Tabular	0.5	1:5
Non-tabular	0.41	1:5
Domed	0.41	1:4
Pinnacle	0.25	1:2
Wedge	0.33	1:5
Drydock	0.15	1:1
Blocky	0.5	1:5

Table 2.2: Iceberg shape factor and height to draft ratio according to shape class (Environment Canada, Meteorological Service of Canada, 2005).

Most observations regarding the size and shape of an iceberg are made by looking at the sail of the iceberg and not its keel. For this reason, information about the size and shape of the keel must be derived from the information gathered on the sail. This uncertainty makes it impossible to confidently predict the mass of an iceberg; however, several rules of thumb have emerged from empirical studies (Diemand, 2001). One such rule is

$$M = 7.12 \times 10^3 C_s L^2 H,$$

(Rudkin, 2005) where M is the mass of the iceberg in kilograms, C_s is the shape factor, as given in Table 2.2, and L and H are the waterline length and sail height of the iceberg in meters, respectively.

Icebergs have the same layered structured as the ice shelf from which they broke off. This means that they are composed of layers and layers of ice, with the surface

coming from the most freshly fallen snow. In turn, this also means that the density of icebergs is not uniform. The layers near the bottom of the iceberg are more dense than those at the top due to years of compression from the layers above them. Further, as icebergs pass into more temperate waters, they begin to melt at the top surface and along their waterline. The estimated iceberg density used in one particular study that ran iceberg drift simulations (Wagner et al., 2017) was 850 kg/m^3.

2.1.2.1 Drag Coefficients

The most common iceberg drag coefficients used in iceberg drift modelling are form and skin drag coefficients of an iceberg in air and seawater — denoted as C_a and C_w, respectively. There is, as of now, no consensus in the literature on what the drag coefficients of an iceberg actually are. Therefore, these drag coefficients have been used as tunable parameters in several different studies (Turnbull et al., 2015), (Allison et al., 2014). Some values reported are: $C_w = 1.2 \pm 0.2$ (Banke and Smith, 1974), ratios between C_a and C_w depending on the iceberg's geometry or wind speed (Ettle, 1974), and a C_w of 1.14 for icebergs travelling within an area of ocean with a relatively high Reynold's number (Mauviel, 1980). Within this work, we used values of C_a and C_w between lower and upper bounds of 0.5 and 2.5, respectively (Allison et al., 2014).

2.1.3 Decay

When an iceberg is created, its deterioration begins, especially as it moves into warmer waters and is subjected to waves. Among the major forms of deterioration are melting, calving, and splitting.

Melting, as a process of ice loss, is mostly dependent on water temperature and wave action. The importance of melting in an iceberg's total loss of mass depends on the surface to volume ratio, making it more significant for small icebergs than large ones.

Calving is a process in which small pieces of ice break off from the sides of a iceberg — mostly due to waterline undercutting. Not only does this event lead to a loss in mass, but the rapid imbalance that results can also cause the iceberg to roll. This can lead to further ice loss and a change in size, shape, and appearance of the iceberg, making it more difficult to identify and predict.

Splitting, like calving, is a process in which pieces of the iceberg break away; however, when an iceberg breaks into two or more standalone icebergs, this is known as splitting. This is a common occurrence for very large icebergs and can occur from the force of ocean waves, grounding, or collision. In addition, as melting occurs along the waterline of the iceberg and the sides of the sail begin to calve, icebergs have a tendency to split such that the ram, the underwater portion of an iceberg that extends outward, horizontally, beyond the sail, forms its own iceberg — which likely accounts for a large portion of the dome shaped icebergs in the ocean. This is also likely what occurred when the two beacons installed on the saddle shaped iceberg (referenced later) began to diverge.

2.2 Oceans

2.2.1 Response to Wind Forcing

Wind exerts a stress on the surface of the ocean causing waves and further movement of the water within the top 50 m (Talley et al., 2011). At timescales of approximately a day, the ocean reacts to the wind stress with movement known as *inertial currents*. These are a balance of the Coriolis force and the time derivatives of the horizontal water velocities caused by the wind stress. Therefore, assuming advection and pressure gradient forces are small, inertial currents are the solution of the equations

$$\begin{aligned} \frac{\partial u}{\partial t} &= fv \\ \frac{\partial v}{\partial t} &= -fu, \end{aligned} \tag{2.1}$$

where u and v are the zonal and meridional components of ocean current velocity, t is time, and f is the Coriolis frequency given by

$$f = 2\Omega \sin \phi, \tag{2.2}$$

where $\Omega = 7.2921 \times 10^{-5}$ rad/s is the rotation rate of the Earth and ϕ is the latitude.

The layer that is affected by these frictional forces in the ocean, caused by the wind stress, is known as the *Ekman layer*. Within the Ekman layer, the velocity caused by these frictional forces is strongest at the sea surface, decaying exponentially downward (up to a depth of roughly 50 m). Because of acceleration from the Coriolis force, the surface water moves at an angle of roughly 45° to the wind and, due to the difference in frictional forces with depth, the complete structure is a spiral, known as an *Ekman*

spiral.

At timescales longer than several days and at spatial scales of the Rossby radius of deformation, there is a balance between the two horizontal forces: the Coriolis force and the pressure gradient force. This is known as *geostrophy* and can be represented mathematically by

$$\begin{aligned} fv &= \frac{1}{\rho}\frac{\partial p}{\partial x} \\ fu &= -\frac{1}{\rho}\frac{\partial p}{\partial y}, \end{aligned} \tag{2.3}$$

where ρ is the density of seawater, x and y are the zonal and meridional locations, and p is the pressure.

Additionally, there is also a vertical force balance between the vertical pressure gradient and gravity, known as *hydrostatic balance*, that accompanies geostrophic balance. This is

$$0 = -\frac{\partial p}{\partial z} - \rho g, \tag{2.4}$$

where p is pressure, z is the vertical depth, ρ is the density of seawater, and g is the acceleration due to gravity.

2.2.2 Ocean Data

The ocean model used in this work for drift simulations is a high-resolution global model created by the European Centre for Medium-Range Weather Forecasts (ECMWF). The details of this ocean model are listed in Table 2.3.

Product identifier:	GLOBAL_ANALYSIS_FORECAST_PHY_001_024
Spatial resolution:	1/12°; 1 vertical level (surface)
Temporal resolution:	1-hourly mean
Grid:	Regular
Atmospheric forcings:	3-hourly from ECMWF
Ocean model:	NEMO 3.1
Tides:	No
Reanalysis:	No

Table 2.3: Overview of an ECMWF ocean model. (Nouel, 2016).

Additionally, it is stated in the quality information document that accompanies this data set (Nouel, 2016) that surface currents at the mid latitudes are underestimated on average with respect to in-situ measurements of drifting buoys. The underestimation ranges from 20% in strong currents to 60% in weak currents. Due to the lack of high-frequency current measurements at the global scale, the added value of the hourly surface currents has not yet been quantified. However, as the surface forcing is updated every 3 hours, the high-frequency surface currents are expected to be relevant.

The spatial subset of this data that is focused on in this work is between 40 – 60° North and 40 – 60° West in the year 2015. A visualization of this data for ocean current velocity is shown in Figure 2.5.

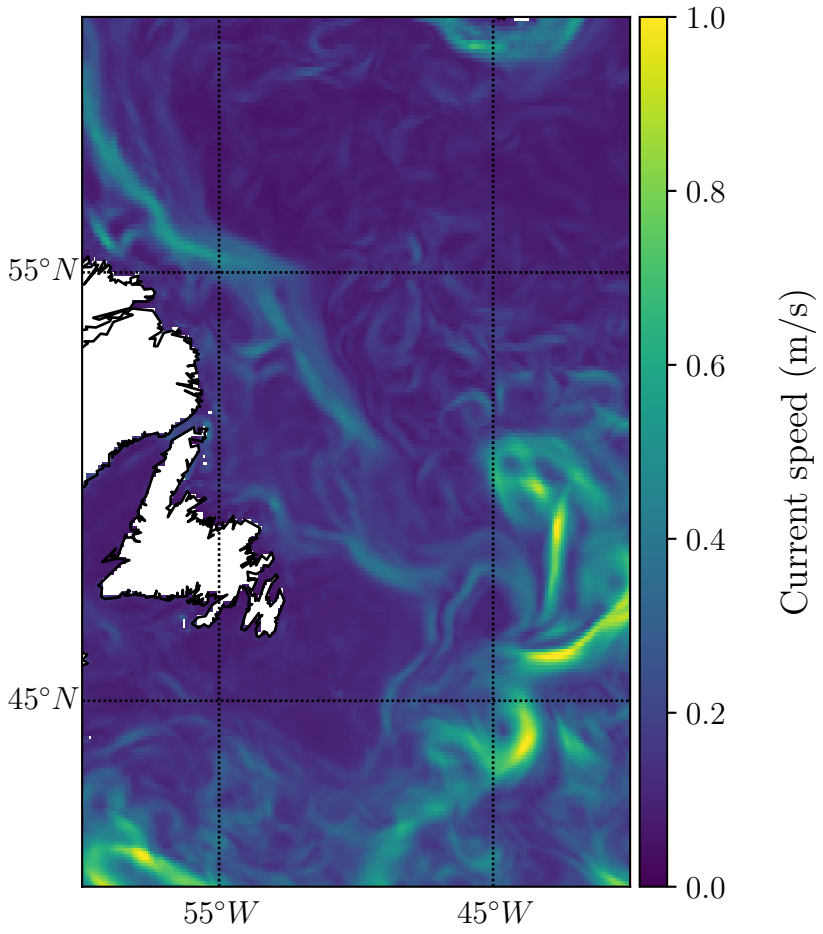

Figure 2.5: Mean ocean current speeds for the month of April, 2015, from an ECMWF ocean model.

2.3 Atmosphere

Like the ocean, large scale flow in the atmosphere is governed by the hydrostatic and geostrophic balances (which involve the vertical balance between the pressure gradient and gravity and the horizontal balance between the pressure gradient and the Coriolis force, respectively) (Vallis, 2006). In contrast though, the atmosphere is largely thermodynamically driven with its primary source of energy coming from solar radiation (Cushman-Roisin, 2011). When solar radiation passes through the air layer, part of it gets absorbed by the land and ocean which re-emits this radiation, but at a longer wavelength, back into the atmosphere causing convection which drives the winds. This phenomenon is especially important for determining the state of the atmosphere at its lowest layer, the *planetary boundary layer*. This is because it usually responds to changes in radiation emitted from the surface in an hour or less. In this layer, wind (and other physical properties such as temperature and moisture) can undergo rapid changes (turbulence) and there is a lot of vertical mixing. Within the planetary boundary layer, the wind is greatly affected by drag along the Earth's surface and turns along the isobars. This is in contrast to the *free atmosphere* (the space in the atmosphere above the planetary boundary layer) where the wind is mostly geostrophic (parallel to the isobars).

Due to the drag from the Earth's surface, there is a gradient in the wind for the first few hundred meters above the surface. In this space, wind speed increases with height, where the wind speed at the surface is zero due to the no-slip condition (Brown, 2001). Furthermore, the wind near the surface is affected by variability in the terrain on the surface causing reductions in wind speed and perturbations to the air

flow in the horizontal and vertical directions causing mixing between the layers. The reduction in wind speed caused by the terrain on the surface is dependent upon the amount of variation in the topography in this terrain. For this reason, the reduction is often greater above land, where there are mountains and large man-made structures, than it is above the ocean. Within the planetary boundary layer, the wind speed can be estimated using the wind power law

$$u = u_r \left(\frac{z}{z_r} \right)^{\alpha} \tag{2.5}$$

where u is the wind speed at a certain height, z, u_r is a known wind speed at a certain reference height, z_r, and

$$\alpha = a - b \log u(z_r) \tag{2.6}$$

is a dimensionless exponent empirically derived through linear regression of wind speed at a reference height and a simultaneously known vertical wind profile (Turnbull et al., 2015) and where typical values for a and b derived from the linear regression are 0.11 and 0.061 in the daytime, and 0.38 and 0.209 at night, respectively (Johnson and Moretti, 1985).

Note that, since the direction of winds will be referred to throughout this work, it is most common to express wind velocities based upon where they originate from (as opposed to where they are heading, as ocean current velocities are expressed). This distinction arises in the difference between Easterly (originating from the East) and Eastward (heading towards the East) — likewise, for Northerly and Northward.

Product identifier:	WIND_GLO_WIND_L4_NRT_OBSERVATIONS_012_003
Spatial resolution:	1/4°; 1 vertical level (10 m)
Temporal resolution:	6-hourly mean
Grid:	Regular
Reanalysis:	No

Table 2.4: Overview of an ECMWF atmospheric model. (Bentamy, 2017).

2.3.1 Atmospheric Data

The first atmospheric model that we tried using for wind velocity data was the global ECMWF model WIND_GLO_WIND_L4_NRT_OBSERVATIONS_012_003, because our ocean model was also from the ECMWF. The details of this atmospheric model are listed in Table 2.4.

The reason, however, that we did not proceed with using this model for our simulations is because there are many missing values in the data. This can be seen when visualizing the wind velocity (see Figure 2.6).

After failing to find suitable atmospheric data from the ECMWF, we had success with a North American Regional Reanalysis (NARR) product. The NARR project is an extension of the National Centers for Environmental Prediction (NCEP) Global Reanalysis which is run over the North American Region. The NARR model uses the high resolution NCEP Eta Model (32 km, 45 layer) together with the Regional Data Assimilation System (RDAS) that, significantly, assimilates precipitation along with other variables. The improvements in the model/assimilation have resulted in a dataset with substantial improvements in the accuracy of temperature, winds, and precipitation compared to the NCEP-DOE Global Reanalysis 2. It provides 10 m

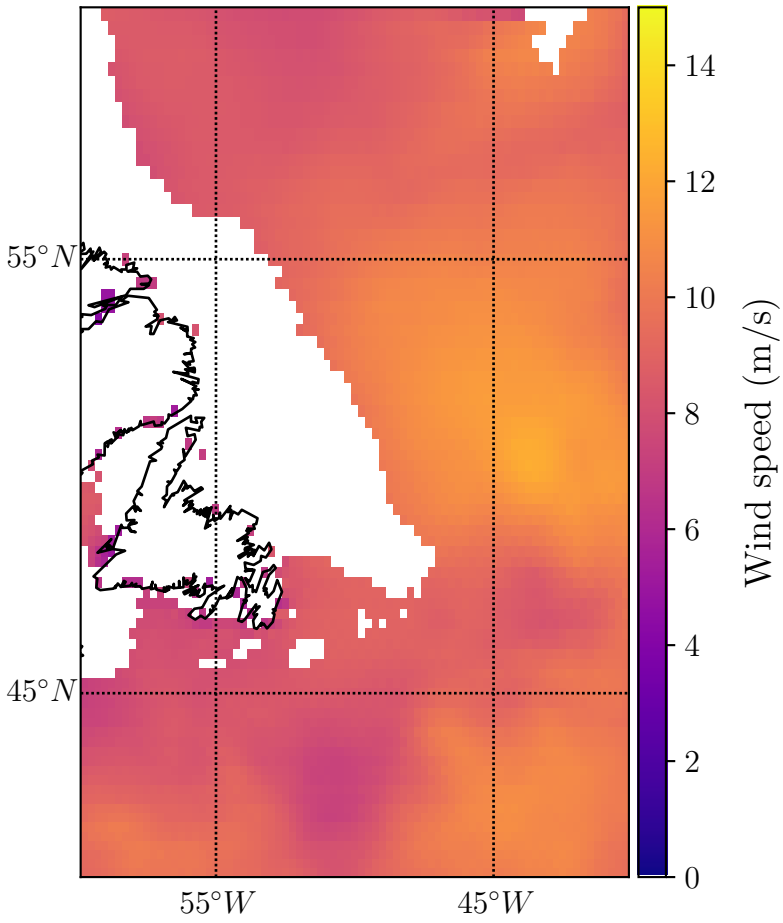

Figure 2.6: Mean wind speeds for the month of April in 2015 from an ECMWF atmospheric model. The white areas in the plot represent the grid cells in the data that have missing values.

Product identifier:	North American Regional Reanalysis
Spatial resolution:	0.3° (32 km); 1 vertical level (10 m)
Temporal resolution:	3-hourly mean
Grid:	Regular
Reanalysis:	Yes

Table 2.5: Overview of the North American Regional Reanalysis (NARR) atmosphere model (Mesinger, 2004).

wind velocities 8-times daily, on a Northern Hemisphere Lambert Conformal Conic grid. The grid resolution is 349x277 which is approximately 0.3 degrees (32 km) resolution at the lowest latitude (Mesinger, 2004). Further information is included in Table 2.5.

When plotting the wind velocity data (Figure 2.7), we see that there are indeed no missing data values in the region of time and space in interested, making this a suitable model for use in our simulations. Furthermore, since this data is reanalysis data, it is likely to have a higher degree of accuracy.

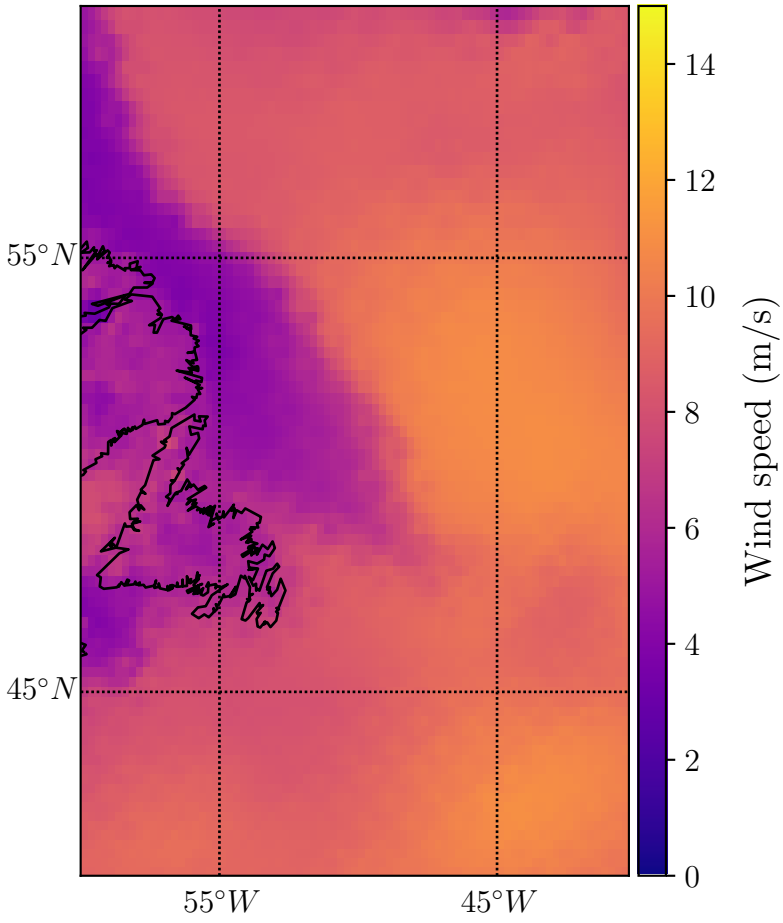

Figure 2.7: Mean wind speeds for the month of April in 2015 from a NARR atmospheric model.

Chapter 3

Iceberg Drift Models

Iceberg drift models fall into three categories: dynamic, statistical, or hybrid. Dynamic drift models predict an iceberg's trajectory using the equations of motion of iceberg drift physics. Statistical models predict an iceberg's trajectory by using recent observations of the iceberg's position to estimate its most probable future positions. Lastly, hybrid drift models are, simply, drift models that use a combination of both dynamic and statistical models to predict an iceberg's trajectory. In this project, we focused on dynamic models exclusively.

Broadly speaking, dynamic drift models are typically written in the form

$$M\frac{d\mathbf{V}}{dt} = -Mf\hat{\mathbf{k}} \times \mathbf{V} + \mathbf{F_p} + \mathbf{F_w} + \mathbf{F_a} + \mathbf{F_r} + \mathbf{F_i} \tag{3.1}$$

where M is the mass of the iceberg, $\mathbf{V}$ is the iceberg velocity, f is the Coriolis parameter, $\mathbf{F_p}$ is the pressure gradient force, $\mathbf{F_w}$ is the water drag force, $\mathbf{F_a}$ is the air drag force, $\mathbf{F_r}$ is the wave radiation force, $\mathbf{F_i}$ is the sea ice drag force, and $-Mf\hat{\mathbf{k}} \times \mathbf{V}$ is the Coriolis force. There are, however, several different variations on this equation

that can be used to model iceberg drift. We first consider one model that assumes the acceleration of the iceberg at any given time is negligible, therefore allowing an analytical solution to be obtained for a simplified version of Equation (3.1). This model is described in (Wagner et al., 2017). The other model that we consider uses an equation very similar to Equation (3.1) in conjunction with a numerical integrator to approximately solve the differential equation over time. This model is described in (Turnbull et al., 2015). It is also the model we chose to use for the case studies seen in Chapter 4.

3.1 Analytical Drift Model

In general, the dynamic model given by Equation (3.1) cannot be solved analytically. This analytical drift model is presented in Wagner (2017). It simplifies Equation (3.1) by making the following key assumptions:

1. The acceleration of the iceberg is small and can be neglected, $\frac{d\mathbf{V}}{dt} \approx 0$.

2. The pressure gradient force can be directly approximated from the ocean velocity, $\mathbf{V_w}$, because of geostrophic ocean currents, $\mathbf{F_p} = Mf\hat{\mathbf{k}} \times \mathbf{V_w}$.

3. The iceberg speed is much smaller than the speed of the surface wind, $|\mathbf{V}| \ll |\mathbf{V_a}|$, where $\mathbf{V_a}$ is the surface wind speed.

4. The drag forces from sea ice and wave radiation are small and can be neglected, $\mathbf{F_r} = \mathbf{F_i} \approx 0$.

5. Vertical variations of the ocean current and wind velocities are small and can be neglected.

6. All icebergs can be approximated as being cuboid.

Reasons for making these assumptions are elaborated upon in (Wagner et al., 2017) and are consistent with the motion of icebergs over time scales of months. By making these assumptions, the water and air drag terms can be simplified to

$$\begin{aligned} \mathbf{F_w} &= \tilde{C}_w|\mathbf{V_w} - \mathbf{V}|(\mathbf{V_w} - \mathbf{V}), \\ \mathbf{F_a} &= \tilde{C}_a|\mathbf{V_a} - \mathbf{V}|(\mathbf{V_a} - \mathbf{V}), \end{aligned} \tag{3.2}$$

with $\tilde{C}_w \equiv \frac{1}{2}\rho_w C_w A_w$ and $\tilde{C}_a \equiv \frac{1}{2}\rho_a C_a A_a$, where C_w and C_a are the drag coefficients of water and air, ρ_w and ρ_a are the densities of water and air, and A_w and A_a are the cross-sectional areas upon which the ocean current and wind velocities act, respectively. Assuming that the mean horizontal length over the long term is

$$\frac{2}{\pi}\int_0^{\pi/2}(W\cos\phi + L\sin\phi)d\phi = \frac{2(L+W)}{\pi}, \tag{3.3}$$

where L and W are the length and width of the iceberg, respectively, and ϕ is the angle of the iceberg face to the driving force, then the long-term averaged cross-sectional areas of the keel and sail of the iceberg can be expressed as

$$A_w = \frac{\rho_i}{\rho_w}\frac{2(L+W)H}{\pi} \tag{3.4}$$

and

$$A_a = \frac{A_w(\rho_w - \rho_i)}{\rho_i}, \tag{3.5}$$

where H is the height of the iceberg. One benefit to modelling the iceberg cross-sectional areas in this way is that it accounts for the cases where the orientation of

the iceberg, with respect to the forces acting upon it, is not known. Therefore, these expressions for the cross-sectional areas of the iceberg were used in every simulation shown in this work.

Under these assumptions, Equation (3.1) simplifies to give

$$0 = -Mf\hat{\mathbf{k}} \times \mathbf{V} + Mf\hat{\mathbf{k}} \times \mathbf{V_w} + \tilde{C}_w|\mathbf{V_w} - \mathbf{V}|(\mathbf{V_w} - \mathbf{V}) + \tilde{C}_w|\mathbf{V_a}|\mathbf{V_a} \tag{3.6}$$

or

$$0 = Mf\hat{\mathbf{k}} \times \Delta\mathbf{V} + \tilde{C}_w|\Delta\mathbf{V}|\Delta\mathbf{V} + \tilde{C}_a|\mathbf{V_a}|\mathbf{V_a}, \tag{3.7}$$

where $\Delta\mathbf{V} \equiv \mathbf{V_w} - \mathbf{V}$ and $\mathbf{V_a} \approx \mathbf{V_a} - \mathbf{V}$. This allows introduction of two dimensionless quantities:

$$\begin{aligned} \Lambda_w &\equiv \frac{\tilde{C}_w|\Delta\mathbf{V}|}{Mf}, \\ \Lambda_a &\equiv \frac{\tilde{C}_a|\mathbf{V_a}|^2}{Mf|\Delta\mathbf{V}|}, \end{aligned} \tag{3.8}$$

which represent the magnitudes of the air and water drag relative to the Coriolis force, respectively. This, then, allows Equation (3.7) to be written as

$$0 = \hat{\mathbf{k}} \times \Delta\hat{\mathbf{V}} + \Lambda_w\Delta\hat{\mathbf{V}} + \Lambda_a\hat{\mathbf{V}}_a, \tag{3.9}$$

with unit vectors $\Delta\hat{\mathbf{V}} \equiv \Delta\mathbf{V}/|\Delta\mathbf{V}|$ and $\hat{\mathbf{V}}_\mathbf{a} \equiv \mathbf{V_a}/|\mathbf{V_a}|$. Now, Equation (3.9) can be rearranged as

$$\mathbf{V} = \mathbf{V_w} + \gamma(-\alpha\hat{\mathbf{k}} \times \mathbf{V_a} + \beta\mathbf{V_a}), \tag{3.10}$$

where γ is a dimensionless parameter that represents the proportion of water and air drag acting on the iceberg, given by

$$\gamma = \sqrt{\frac{\tilde{C}_a}{\tilde{C}_w}}, \tag{3.11}$$

and α and β are also dimensionless parameters, given by

$$\begin{aligned} \alpha &\equiv \frac{\sqrt{1+4\Lambda^4}-1}{2\Lambda^3}, \\ \beta &\equiv \frac{1}{2\Lambda^3}\sqrt{1+4\Lambda^4\sqrt{1+4\Lambda^4}-3\Lambda^4-1}, \end{aligned} \tag{3.12}$$

with

$$\Lambda \equiv \sqrt{\Lambda_w \Lambda_a} = \frac{\gamma C_w |\mathbf{V_a}|}{\pi f S} \tag{3.13}$$

and $S = \frac{LW}{L+W}$ as the horizontal mean length of the iceberg.

3.1.1 Numerical Analysis of α and β

While re-implementing the numerical method described in Wagner et al. (2017), we discovered a numerical issue that was of interest in the context of scientific computing. The parameters α and β from Equation (3.12) are functions of a parameter, Λ, given in Equation (3.13) that is always positive but, occasionally, may be of small value. This is shown in Figure 3.1.

In the expression for α, a loss of numerical accuracy can occur when

$$1 - \sqrt{1+\Lambda^4} \tag{3.14}$$

is small. Similarly, difficulties arise in accurately computing

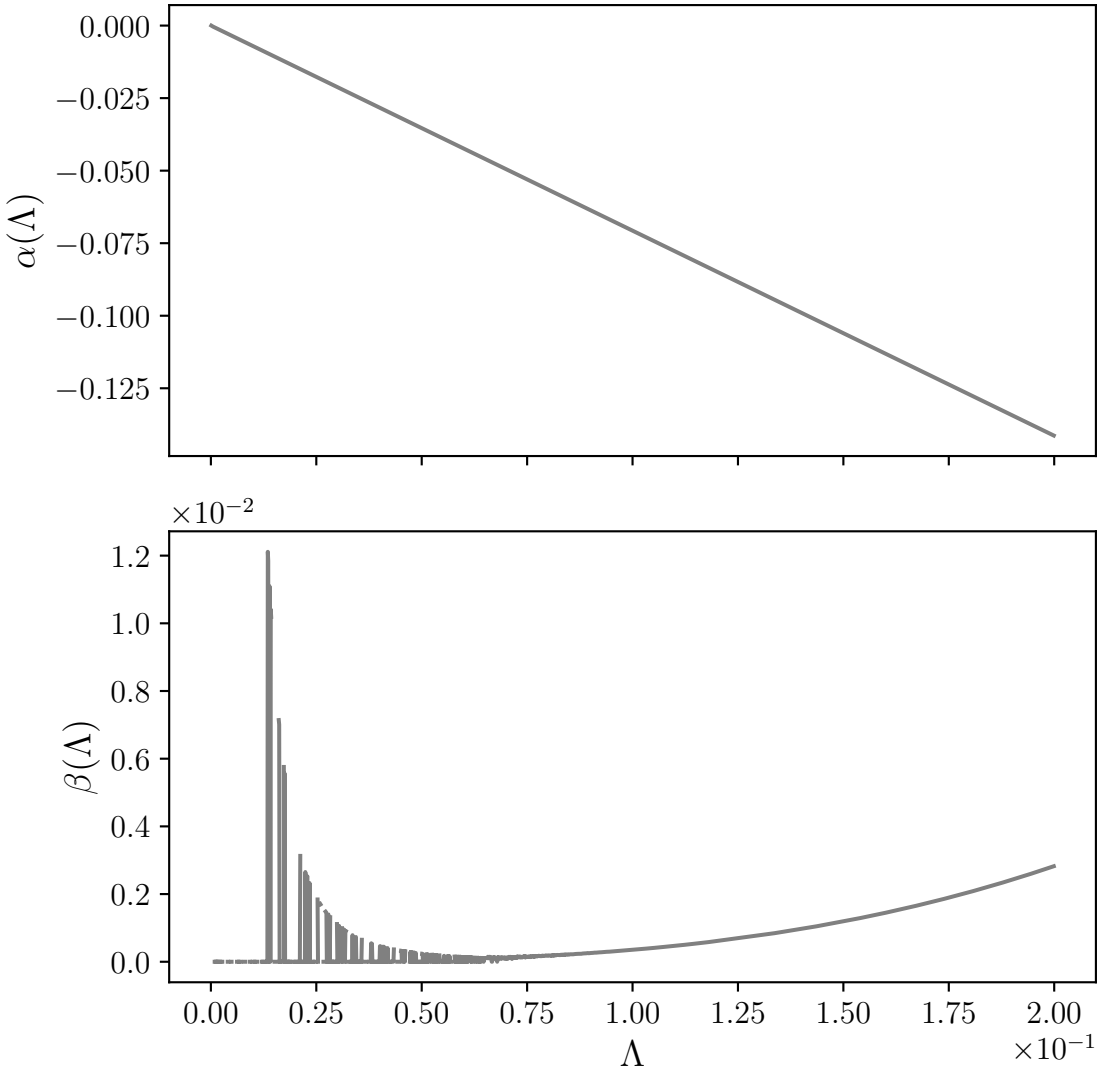

Figure 3.1: Numerical instabilities in functions $\alpha(\Lambda)$ and $\beta(\Lambda)$ for small values of Λ due to round-off error.

$$(1+\Lambda^4)\sqrt{1+4\Lambda^4} - 3\Lambda^4 - 1 \tag{3.15}$$

in the expression for β, as Λ approaches zero. To fix this issue, we began by taking the Taylor approximation of $\sqrt{1+x}$

$$\sqrt{1+x} = 1 + \frac{x}{2} + \sum_{k=2}^{\infty} \frac{(-1)^{k+1}(2k-3)!}{2^{2k-2}(k-2)!k!} x^k \tag{3.16}$$

to directly reduce round-off errors in computing the square root when x is small. Using this approximation to express α for small Λ gives

$$\alpha \approx \frac{\sqrt{2}}{2}(-\Lambda + \frac{\Lambda^5}{4} - \frac{\Lambda^9}{8} + \frac{5\Lambda^{13}}{64} - \frac{7\Lambda^{17}}{128} + O(\Lambda^{21})). \tag{3.17}$$

Similarly, for small Λ, we have

$$\beta \approx \frac{\sqrt{2}}{4}(\Lambda^3 - \frac{3\Lambda^7}{8} + \frac{27\Lambda^{11}}{128} - \frac{143\Lambda^{15}}{1024} + \frac{3315\Lambda^{19}}{32768} - \frac{20349\Lambda^{23}}{262144} + \frac{260015\Lambda^{27}}{4194304} - \frac{1710855\Lambda^{31}}{33554432} + \frac{92116035\Lambda^{35}}{2147483648} - \frac{744762895\Lambda^{39}}{17179869184} + O(\Lambda^{43})), \tag{3.18}$$

where we keep fewer terms in the expansion for α than in that for β because the computation of β is more ill-conditioned.

In order to also avoid computing large exponents of Λ, we can further factor these expressions using Horner's method. This gives

$$\alpha \approx \Lambda(\Lambda^4(\Lambda^4(\Lambda^4(-0.0386699020961393\Lambda^4 + 0.055242717280199) - 0.0883883476483184) + 0.176776695296637) - 0.707106781186548) \tag{3.19}$$

and

$$\begin{aligned}\beta \approx \Lambda^3(\Lambda^4(\Lambda^4(\Lambda^4(\Lambda^4(\Lambda^4(\Lambda^4(\Lambda^4(\Lambda^4(\Lambda^4(-0.0138698305427678\Lambda^4+\\ 0.0129890788831978) - 0.0151656272365985)+\\ 0.0180267866272764) + 0.0219176256311202)-\\ 0.0274446790511418) + 0.0357675015202851)-\\ 0.0493731785691779) + 0.0745776683282687)-\\ 0.132582521472478) + 0.353553390593274), \quad (3.20)\end{aligned}$$

which is beneficial because the largest power of Λ that must be computed in these expressions is the fourth power.

Now, if we look at the absolute difference between our naive implementations and our new Taylor approximated and Horner evaluated functions (Figures 3.2 and 3.3), we can see the difference in how they behave. This allows us to use the functions α and β for any positive values of Λ without getting unexpected values due to numerical round-off errors.

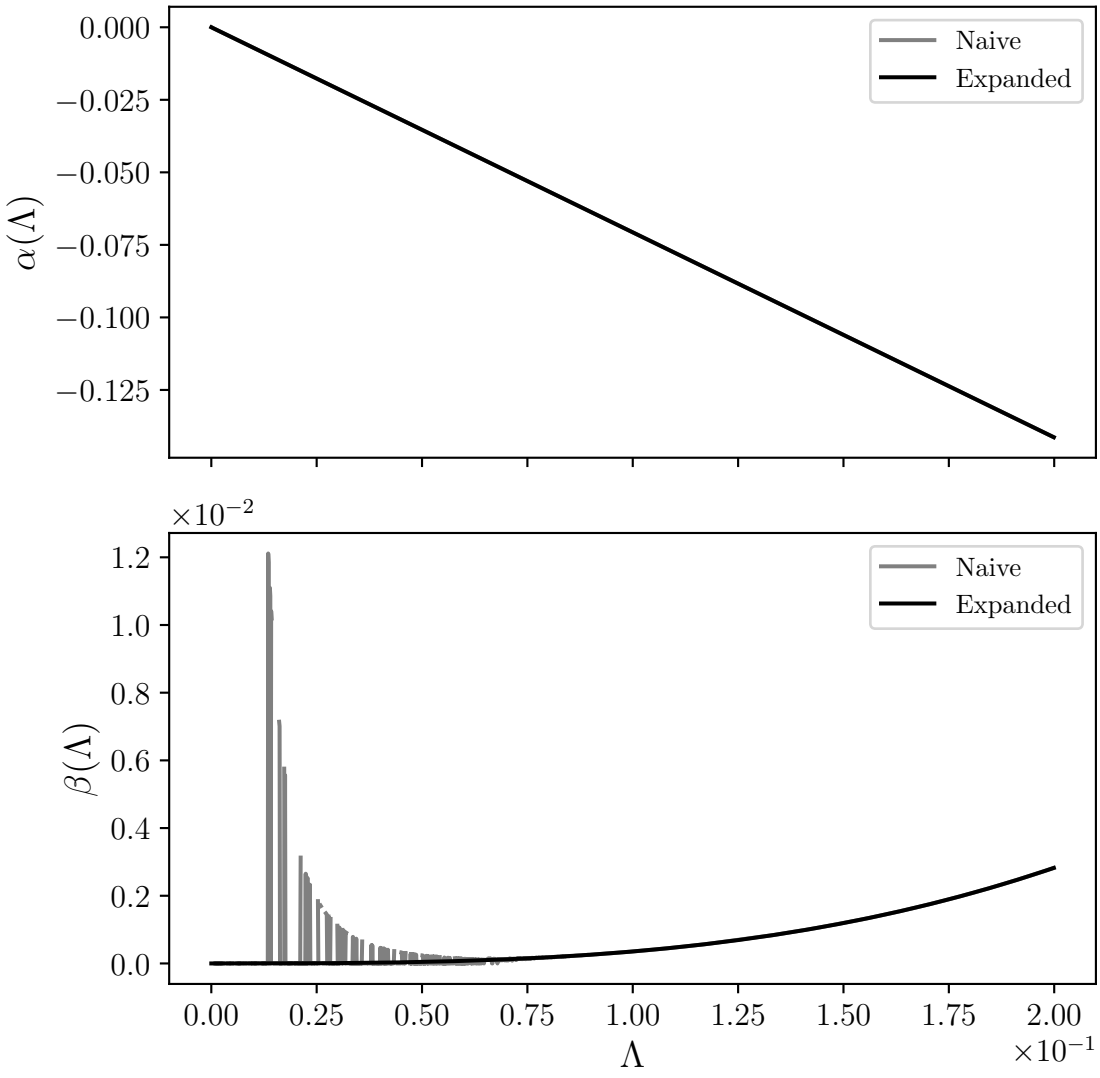

Figure 3.2: Naive versus Taylor Series expanded implementations of $\alpha(\Lambda)$ and $\beta(\Lambda)$.

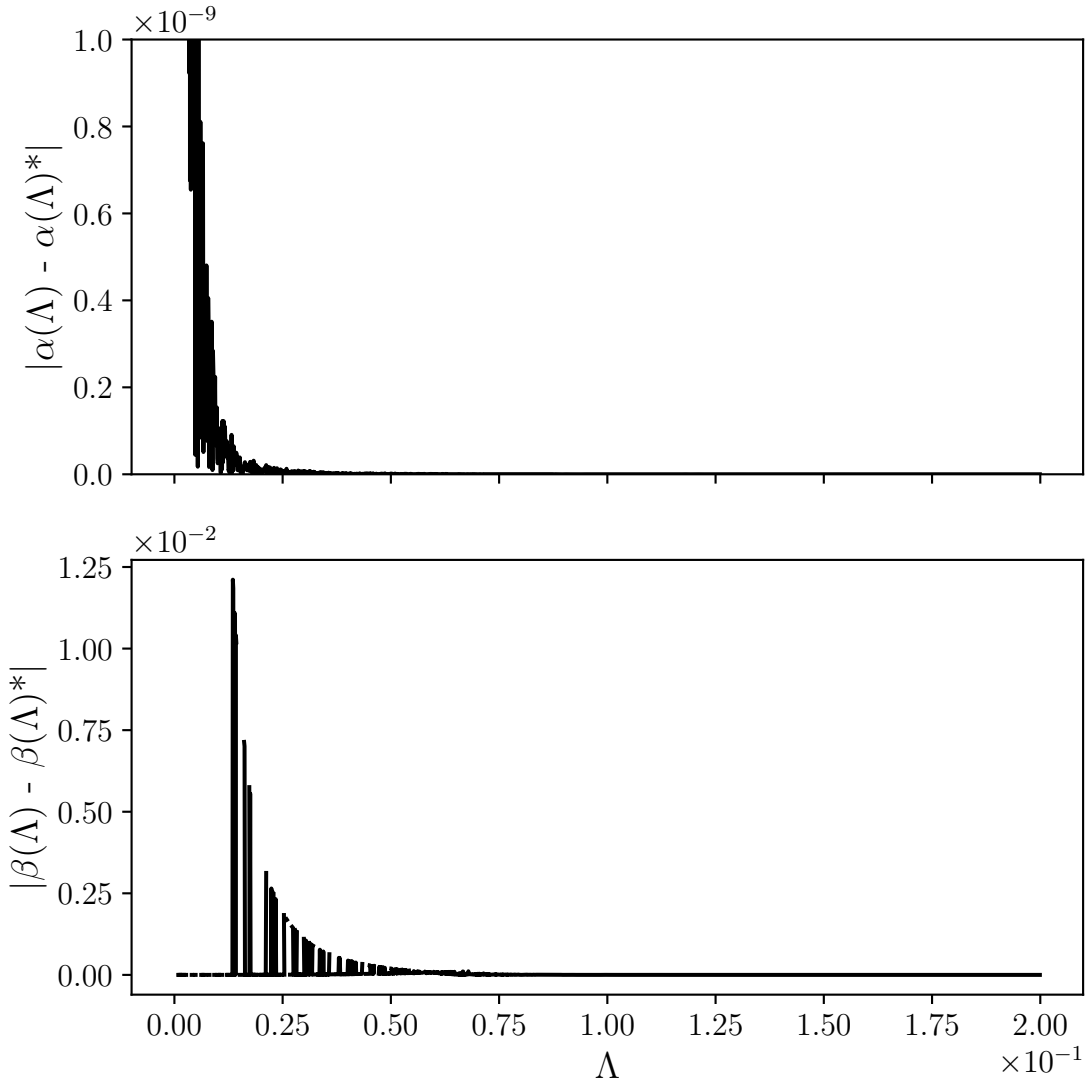

Figure 3.3: Absolute difference of naive and Taylor Series expanded implementations of $\alpha(\Lambda)$ and $\beta(\Lambda)$.

3.2 Newtonian Drift Model

As an alternative to making the simplifying approximations as described in the analytical model of (Wagner et al., 2017), we also investigated solving Equation (3.1) numerically. This is the method that is used in Chapter 4 to predict the trajectory of the icebergs.

The drift model used during Shell's Greenland coring campaign in 2012 (Turnbull et al., 2015) also follows from the fundamental iceberg drift equation of motion shown in Equation (3.1). However, as the timescale of drifting considered was on the scale of a few hours to a few days (versus timescales of months for Wagner et al. (2017)), the final equation of motion for this model differs significantly from that of the Wagner et al. model.

The assumptions made for this model are as follows:

1. Wave forcing is negligible, because it's inclusion made no improvement to the forecast quality, giving $\mathbf{F_r} \approx 0$.

2. Sea ice forcing is also negligible, because no sea ice was observed during the campaign, giving $\mathbf{F_i} \approx 0$.

3. Tidal currents for the coring region near Cape North were deemed significant and were, thus, accounted for, but for this region only.

4. Sea surface slope was neglected because it was not possible for them to measure these during this campaign.

5. For icebergs of tabular, non-tabular, dome, wedge, and blocky shape, skin drag on the top face of the iceberg was significant and was, therefore, accounted for.

6. All icebergs had either triangular or semi-elliptical keels.

7. Skin drag across the bottom surface of the iceberg for all iceberg shapes was ignored, because the cross-sectional area of the keel's tip was negligible.

It is important to note, however, that there are some limitations with these assumptions. In particular, with regards to shape and drag. In this work, when this drift model was used for icebergs for which no keel information was provided, skin drag on the bottom face of the iceberg was accounted for. In addition, since there does not seem to be any consensus on specific drag coefficient values (see Section 2.1.2.1), the drag coefficient were used as tunable parameters within the range of 0.5 and 2.5 (Allison et al., 2014).

With these assumptions, Equation (3.1) simplifies to

$$M\frac{d\mathbf{V}}{dt} = \mathbf{F_a} + \mathbf{F_w} + \mathbf{F_C} + \mathbf{F_{wp}}, \tag{3.21}$$

where M and $\mathbf{V}$ are the mass and the velocity of the iceberg; respectively, t is the time, and $\mathbf{F_a}$, $\mathbf{F_w}$, $\mathbf{F_C}$, and $\mathbf{F_{wp}}$ are the forces of air, water, Coriolis, and water pressure; respectively. For the force of air drag on the iceberg, we write

$$\mathbf{F_a} = (0.5\rho_a C_a A_s + \rho_a C_{da} A_t)|\mathbf{V_a} - \mathbf{V}|(\mathbf{V_a} - \mathbf{V}), \tag{3.22}$$

where ρ_a, C_a, C_{da}, and $\mathbf{V_a}$ are the density, drag coefficient, skin drag coefficient, and velocity of the air; respectively, and A_s, A_t are the area of the sail and the top of the iceberg; respectively. Similarly, we have

$$\mathbf{F_w} = 0.5\rho_w(C_w \sum_n A_k(n)|\mathbf{V_w}(n) - \mathbf{V}|(\mathbf{V_w}(n) - \mathbf{V}) + C_{dw}A_b|\mathbf{V_w} - \mathbf{V}|(\mathbf{V_w} - \mathbf{V})), \tag{3.23}$$

or, summing over depths,

$$\mathbf{F_w} = 0.5\rho_w(C_wA_k + C_{dw}A_b)|\mathbf{V_w} - \mathbf{V}|(\mathbf{V_w} - \mathbf{V}), \tag{3.24}$$

where ρ_w, C_w, C_{dw}, and $\mathbf{V_w}$ are the density, drag coefficient, skin drag coefficient, and velocity of the water; respectively, and A_k, A_b are the area of the keel and the bottom of the iceberg; respectively, and n is the depth level. As above,

$$\mathbf{F_C} = -2M\Omega \sin\phi \hat{\mathbf{k}} \times \mathbf{V}, \tag{3.25}$$

where $\mathbf{F_C}$ is the Coriolis Force, Ω is the angular speed of Earth, ϕ is the iceberg's latitude, and $\hat{\mathbf{k}}$ is the unit vector perpendicular to the Earth's surface. Finally,

$$\mathbf{F_{wp}} = M(\frac{d\bar{\mathbf{V}}_\mathbf{w}}{dt} + f \times \bar{\mathbf{V}}_\mathbf{w}), \tag{3.26}$$

where $\bar{\mathbf{V}}_\mathbf{w}$ is the mean water velocity along the iceberg's keel and $f = 2\Omega \sin\phi$ is the Coriolis parameter.

For this drift model, a free body diagram of an iceberg that is approximately in equilibrium is shown in Figure 3.4. As usual, the forces of water and air drag are the dominant forces; however here, the iceberg is not moving in either of those directions due to the Coriolis force caused by the rotation of the Earth. It should be noted too that the velocity of the wind is usually at least an order of magnitude greater than the velocity of the current. The reason that the air drag force does not dominate

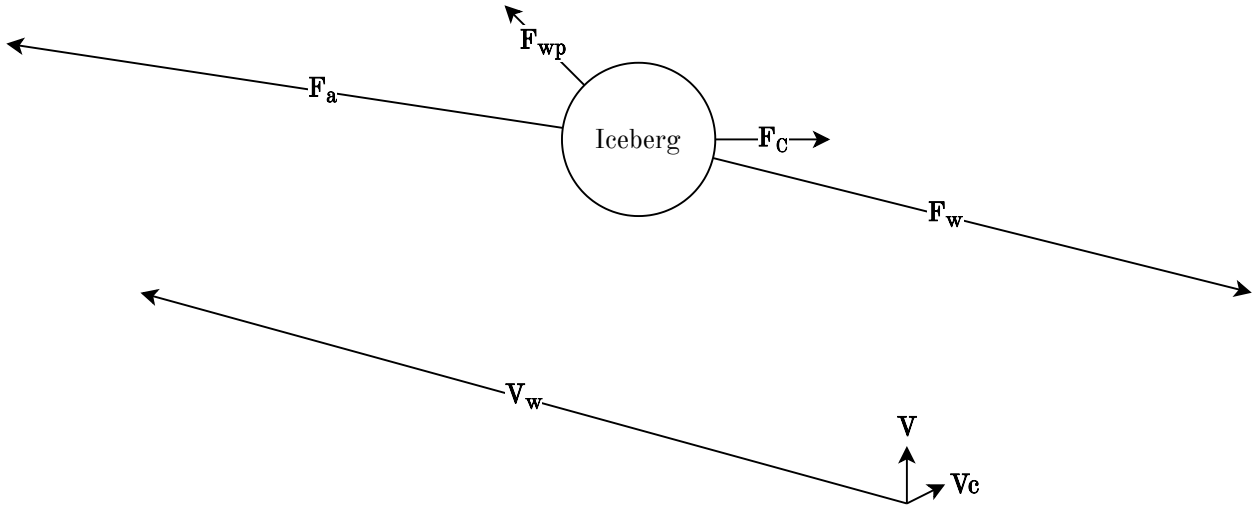

Figure 3.4: Free body diagram for an iceberg that is roughly in equilibrium where $\mathbf{F_a}$, $\mathbf{F_w}$, $\mathbf{F_C}$, and $\mathbf{F_{wp}}$ represent the air drag, water drag, Coriolis, and water pressure gradient forces, respectively, and $\mathbf{V}$, $\mathbf{V_c}$, and $\mathbf{V_w}$ represent the velocity of the iceberg, current, and wind, respectively.

the water drag force is because the density of air is much smaller than the density of water.

3.3 Time Stepping Methods

In order to approximate the velocity of the iceberg from Equation (3.21), numerical integration is needed. Therefore, we tried several different classes of time-stepping methods such as single step, linear multi-step, and predictor-corrector methods to see how they affected the speed, stability, and accuracy of the solution. As shown in Figure 3.5, for simulations with a 300 second time step and total integration time of 24 hours, the accuracy of the solution does not vary significantly between time

steppers. They are also all stable for most simulations; therefore, we chose to run our simulations using the forward Euler method for its speed and ease of implementation.

3.3.1 Runge-Kutta Methods

Considering the first-order differential equation,

$$y' = f(t, y), \tag{3.27}$$

the numerical approximation to the solution of this equation using Runge-Kutta methods is

$$y_{n+1} = y_n + h \sum_{i=1}^{r} p_i k_i, \tag{3.28}$$

where

$$k_i = f(x_i + s_i h,\ y_n + h \sum_{j=1}^{r} q_{ij} k_j) \tag{3.29}$$

and h is the time step. One way to represent this system is using a Butcher tableau, as shown in Table 3.1, where the relation between the coefficients s_i and q_{ij} is given by

$$s_i = \sum_{j=1}^{r} q_{ij},\ i = 1, 2, \ldots r. \tag{3.30}$$

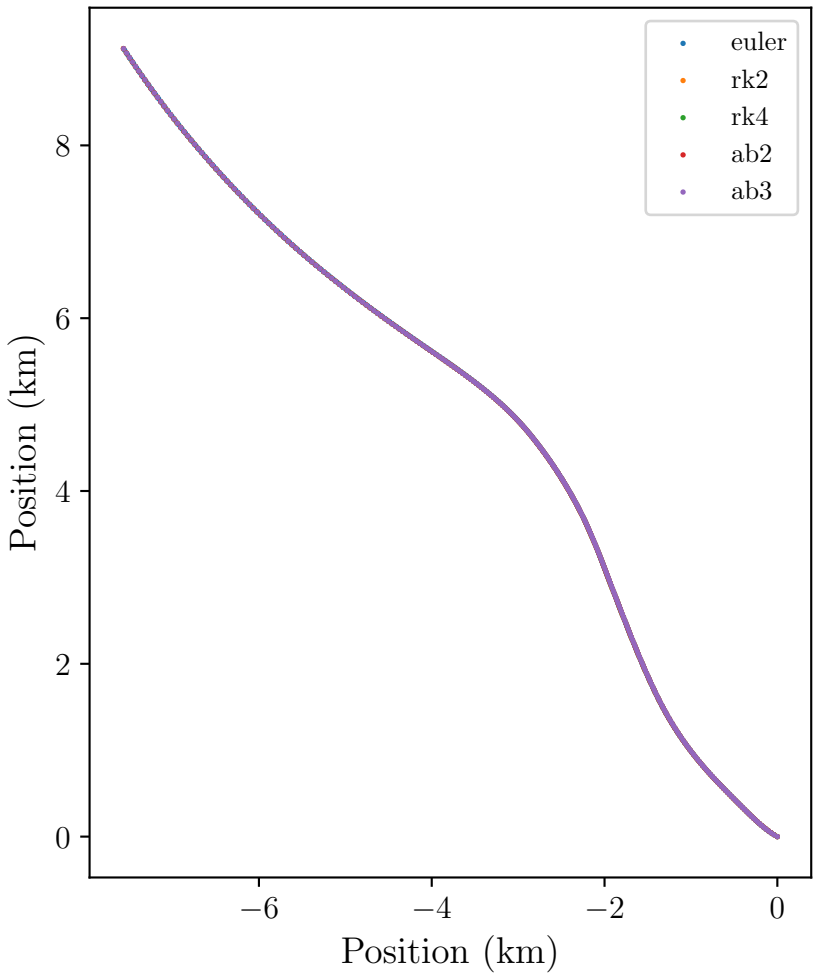

Figure 3.5: Iceberg drift track simulation under the same conditions except varying the numerical time stepper. Here "euler" is the forward Euler method, "rk2" is the second-order Runge-Kutta method, "rk4" is the fourth order Runge-Kutta method, "ab2" is the second-order Adams-Bashforth method, and "ab3" is the third-order Adams-Bashforth method.

s_1	q_{11}	q_{12}	$\dots$	q_{1r}
s_2	q_{21}	q_{22}	$\dots$	q_{2r}
$\vdots$	$\vdots$	$\vdots$		$\vdots$
s_r	q_{r1}	q_{r2}	$\dots$	q_{rr}
	p_1	p_2	$\dots$	p_r

Table 3.1: Butcher tableau for a Runge-Kutta method

0	0	0
$\frac{1}{2}$	$\frac{1}{2}$	0
	0	1

Table 3.2: Butcher tableau for the explicit midpoint method.

The two Runge-Kutta methods that we used were a second-order Runge-Kutta method called the explicit midpoint method and a fourth-order Runge-Kutta method.

3.3.1.1 Second-order Runge-Kutta Method (Explicit Midpoint)

The explicit midpoint method is a second-order Runge-Kutta method. The local error at each step of the midpoint method is of order $O(h^3)$, giving a global error of order $O(h^2)$. Thus, while more computationally intensive than Euler's method, the midpoint method's error generally decreases faster as $h \to 0$. The Butcher tableau for this method is given in Table 3.2.

0	0	0	0	0
$\frac{1}{2}$	$\frac{1}{2}$	0	0	0
$\frac{1}{2}$	0	$\frac{1}{2}$	0	0
1	0	0	1	0
	$\frac{1}{6}$	$\frac{1}{3}$	$\frac{1}{3}$	$\frac{1}{6}$

Table 3.3: Butcher tableau for the fourth-order Runge-Kutta method

3.3.1.2 Fourth-order Runge-Kutta Method

The RK4 method is a fourth-order method, meaning that the local truncation error is of the order of $O(h^5)$, while the total accumulated error is of the order of $O(h^4)$. The Butcher tableau for this method is given in Table 3.3.

3.3.2 Linear Multi-step Methods

Multi-step methods use information from the previous steps to calculate the next value. Considering again the first-order differential equation,

$$y' = f(t, y), \tag{3.31}$$

a linear multi-step method uses a linear combination of y_i and $f(t_i, y_i)$ to calculate the value of y for the current step. Therefore, a linear multi-step method is a method of the form

$$\sum_{j=0}^{s} a_j y_{n+j} = h \sum_{j=0}^{s} b_j f(t_{n+j}, y_{n+j}), \tag{3.32}$$

where $a_s = 1$ and we solve for y_{n+j} given values $y_n,\ y_{n+1},\ \ldots,\ y_{n+s-1}$. The coefficients $a_0,\ a_1,\ \ldots,\ a_{s-1}$ and $b_0,\ b_1,\ \ldots,\ b_{s-1}$ determine the method.

3.3.2.1 Adams-Bashforth

The Adams-Bashforth methods are linear multi-step methods where the coefficients are $a_{s-1} = -1$ and $a_{s-2} = \cdots = a_0 = 0$ and the b_j are chosen such that the methods have order s.

The Adams-Bashforth methods with $s = 1,\ 2,\ 3$ are (Hairer, 1987),

$$\begin{aligned}
y_{n+1} &= y_n + hf(t_n, y_n) \\
y_{n+2} &= y_{n+1} + h\left(\frac{3}{2}f(t_{n+1}, y_{n+1}) - \frac{1}{2}f(t_n, y_n)\right) \\
y_{n+3} &= y_{n+2} + h\left(\frac{23}{12}f(t_{n+2}, y_{n+2}) - \frac{16}{12}f(t_{n+1}, y_{n+1}) + \frac{5}{12}f(t_n, y_n)\right)
\end{aligned} \tag{3.33}$$

and are $O(h^s)$ accurate.

The Adams-Bashforth method with $s = 1$ is known as the explicit Euler method. Since it is order 1, the local truncation error is $O(h^2)$. It is simple and fast but may lack stability and accuracy. However, since accuracy and stability did not vary much between the various time-stepping methods we tried (see Figure 3.5), this method was suitable for most of our simulations. The other Adams-Bashforth methods that we tried were methods where $s = 2$ and $s = 3$.

Chapter 4

Results

4.1 Validation & Verification

In order to help verify that the physics in the drift model and the programming implementation were accurate, we tested the model with various artificial metocean inputs designed to simplify the equations of motion. These inputs were: no current with constant wind, no wind with constant current, no wind or current, and constant wind and current. The results of these tests all matched the expected behaviour and, therefore, helped verify our model.

The test case of no current and constant wind, shown in Figure 4.1, produced results that showed there was constant forcing from the air drag in the direction of the wind, constant forcing from the water drag in the direction opposite the direction of iceberg motion, a small but constant Coriolis force perpendicular to the direction of iceberg motion, and no pressure gradient force.

The test case of no wind and constant current, shown in Figure 4.2, produced

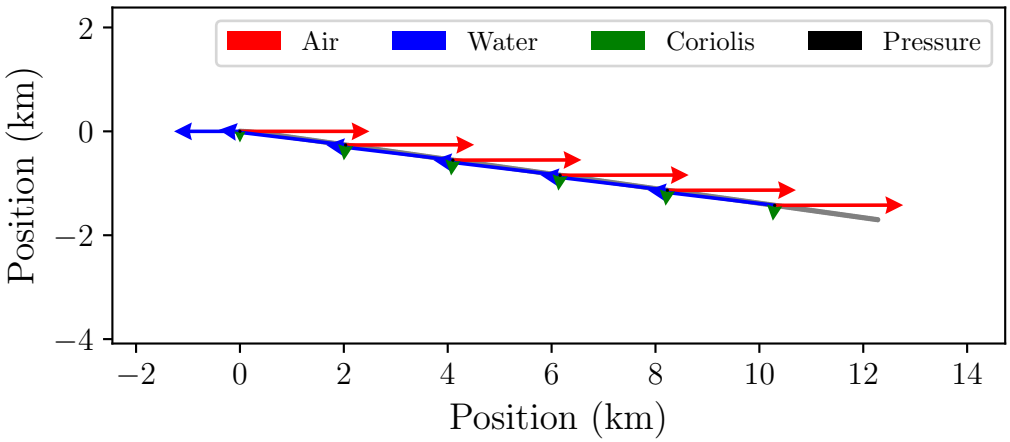

Figure 4.1: Iceberg drift simulation with a constant current velocity of (0, 0) m/s, constant wind velocity of (10, 0) m/s, and an initial iceberg velocity of (0.2, 0) m/s. The arrows represent the air, water, Coriolis, and pressure gradient force vectors at various points throughout the simulation.

results that showed there was constant forcing from the water drag in the direction of the current, constant forcing from the air drag in the direction opposite the direction of iceberg motion, and constant Coriolis and pressure gradient forces perpendicular to the direction of iceberg motion, that are equal in magnitude but opposite in direction.

The test case of no current or wind and an initial non-zero iceberg velocity, shown in Figure 4.3, produced results that showcase the Coriolis effect well. There was a constant water drag force, a constant but very small air drag force, in the direction opposite the direction of iceberg motion, a constant Coriolis force perpendicular to the direction of iceberg motion, and no pressure gradient force.

The test case of constant current and constant wind, shown in Figure 4.4, produced results that showed there was constant forcing from the air drag in the direction of

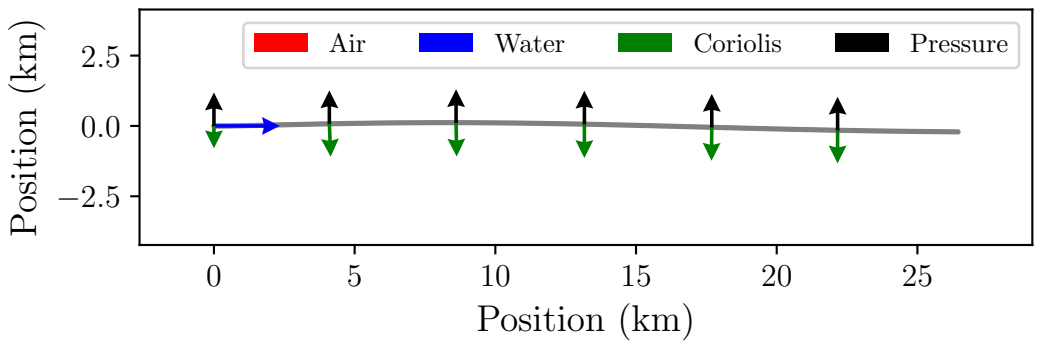

Figure 4.2: Iceberg drift simulation with a constant current velocity of (0.3, 0) m/s, constant wind velocity of (0, 0) m/s, and an initial iceberg velocity of (0.2, 0) m/s. The arrows represent the air, water, Coriolis, and pressure gradient force vectors at various points throughout the simulation.

the wind, constant forcing from the water drag in the direction opposite the direction of iceberg motion, a small but constant Coriolis force perpendicular to the direction of iceberg motion, and no pressure gradient force.

4.1.1 Varying Size and Shape

Iceberg observations normally estimate the iceberg's geometry by placing them into size and shape classes based on the best guess of which classes it belongs to during observation. These size and shape classes, shown in Tables 2.1 and 2.2; respectively, have values that govern the waterline length, sail height, and sail height to draft ratios. These values are important in the context of drift models (as discussed in Chapter 3) because they determine the cross-sectional areas of the iceberg, above and below the surface, that the water and air drag forces act upon as well as their mass.

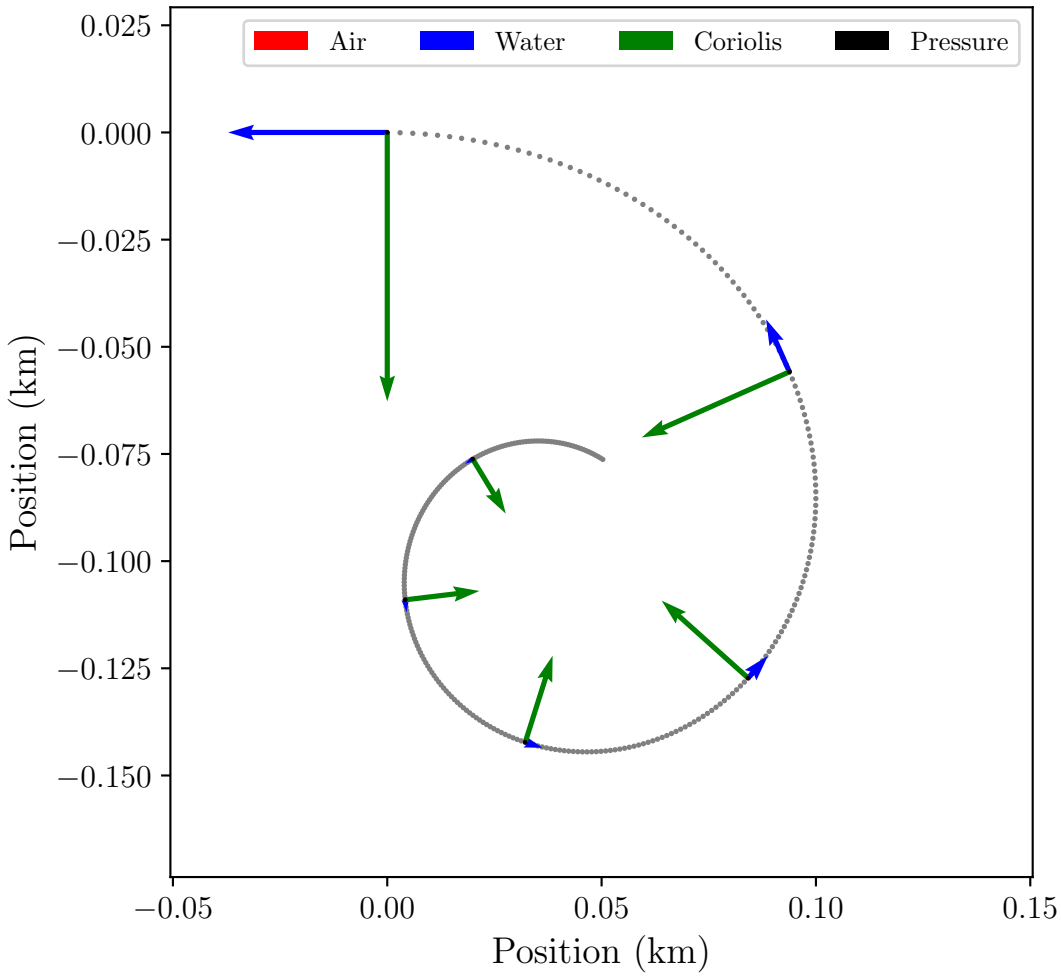

Figure 4.3: Iceberg drift simulation with a constant current velocity of (0, 0) m/s, constant wind velocity of (0, 0) m/s, and an initial iceberg velocity of (0.1, 0) m/s. The arrows represent the air, water, Coriolis, and pressure gradient force vectors at various points throughout the simulation.

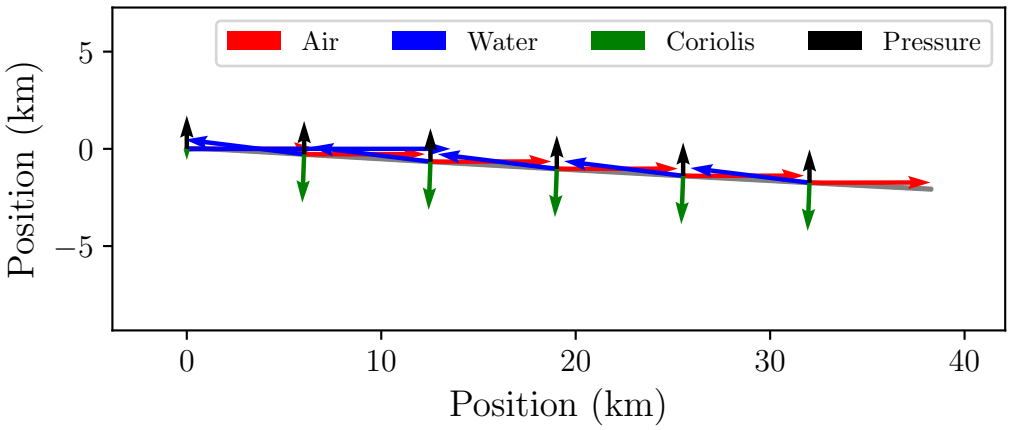

Figure 4.4: Iceberg drift simulation with a constant current velocity of (0.3, 0) m/s, constant wind velocity of (10, 0) m/s, and an initial iceberg velocity of (0.1, 0) m/s. The arrows represent the air, water, Coriolis, and pressure gradient force vectors at various points throughout the simulation.

As shown in Figure 4.5, the trajectory of an iceberg can change significantly according to which size class it is placed in. Furthermore, since the range of dimensions in each class is fairly large, the trajectory can also vary significantly depending on where in the range its true dimensions lie.

Likewise, the shape class in which the iceberg is placed is also important since this will affect the height to draft ratio which, in turn, affects the cross-sectional areas of the iceberg that the water and air drag forces act upon. As shown in Figure 4.6, the trajectory of the iceberg can vary greatly depending on which shape class it is sorted into.

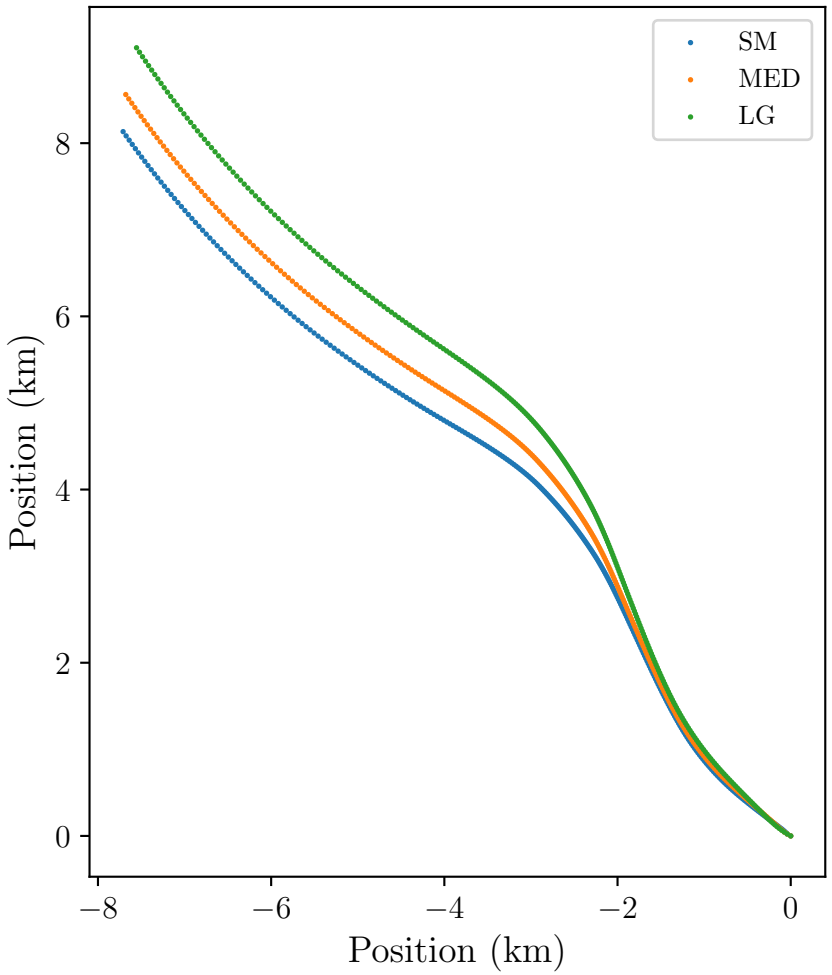

Figure 4.5: Iceberg drift tracks simulated with different sizes of iceberg over a 24 hour period (SM, MED, and LG refer to size classes seen in Table 2.1). General direction of drift is from the bottom right corner to the top left corner of the figure.

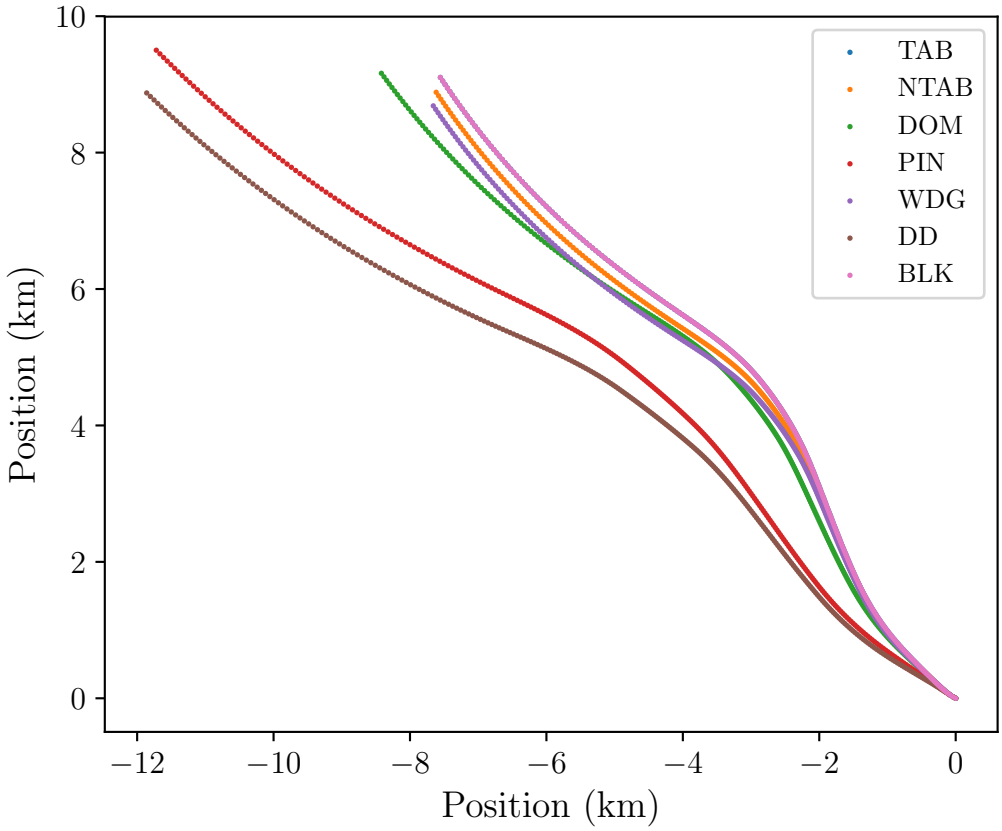

Figure 4.6: Iceberg drift tracks simulated with different shapes of iceberg over a 24 hour time period (TAB, NTAB, DOM, PIN, WDG, DD, and BLK refer to shape classes seen in Table 2.2). General direction of drift is from the bottom right corner to the top left corner of the figure.

4.2 Statoil-ArcticNet Expedition 2015

In order to verify a drift model's ability to accurately predict an iceberg's drift under real-world conditions, it is necessary to have accurate observational measurements of iceberg drift (with high temporal resolution) and accurate current and wind velocity data; this is where the Statoil-ArcticNet research expedition of 2015 is valuable. During this expedition, they placed time and location transmitting beacons onto two icebergs and took measurements of current and wind velocities using an ADCP and AVOS device, respectively. This data is used later in this work for iceberg drift simulations.

4.2.1 The Expedition

The Canadian research icebreaker CCGS Amundsen left its home port in Quebec City on April 17th, 2015, for the first segment of a seven segment expedition. During this first leg, metocean, sea ice, iceberg, and environmental data were collected — in particular, wind and ocean current velocities and the coordinates of two icebergs over time. The Amundsen returned to port in Quebec City on May 4th, 2015, marking the end of its initial 18 day expedition. The location of the Amundsen during Leg 1 of the expedition is shown in Figure 4.7.

To track the coordinates of the two icebergs, four Solara FT-2000 iridium transmitters were used (two per iceberg) — their identification numbers were 204980, 505190, 906790, and 907780. These drift tracks are shown in Figure 4.8.

Beacons 204980 and 906790 were deployed on a saddle shaped iceberg on April 24th, 2015 at roughly 3 PM. A photograph of this iceberg is shown in Figure 4.9.

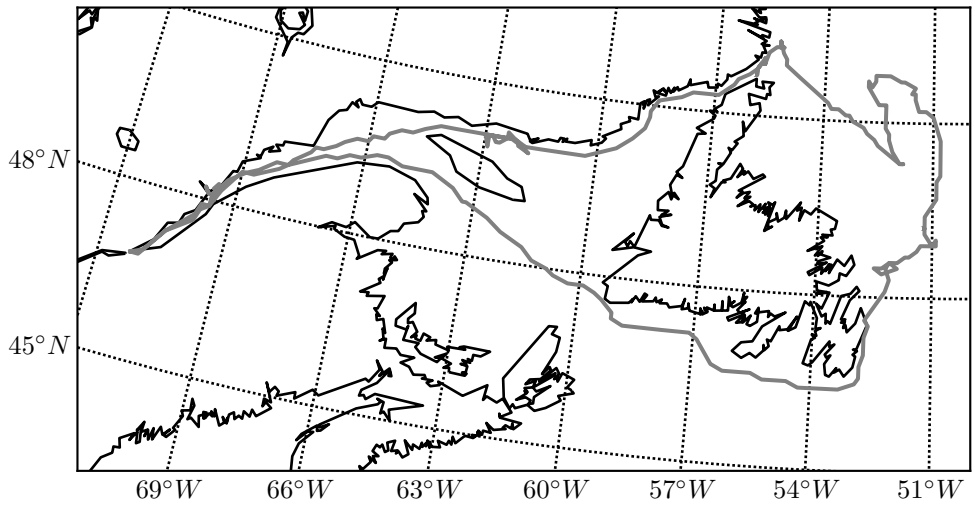

Figure 4.7: Location of the Amundsen during Leg 1 of 2015 research expedition.

In the beginning, the measurement interval was roughly every 30 seconds. Later, the measurement frequency dropped to roughly once an hour. At about 05:40 on April 30, the two beacons began to diverge. It is suspected that 906790 remained on the original iceberg while 204980 either remained on a part of a piece that calved off the original, or fell off the iceberg entirely onto a piece of sea ice, or simply fell into the water. Despite the fact that these beacons were weighted to sink, the latter hypothesis is still possible, considering the variability observed in the beacon's drift in May and June.

Beacons 505190 and 907780 were deployed on a large tabular iceberg at around 7 PM on April 23rd, 2015. A photograph of this iceberg is shown in Figure 4.10. In the beginning, the measurement interval was roughly every 30 seconds. Later, the measurement frequency dropped to roughly once an hour. There was an issue, however, with 907780 as it only transmitted for the first hour and then stopped.

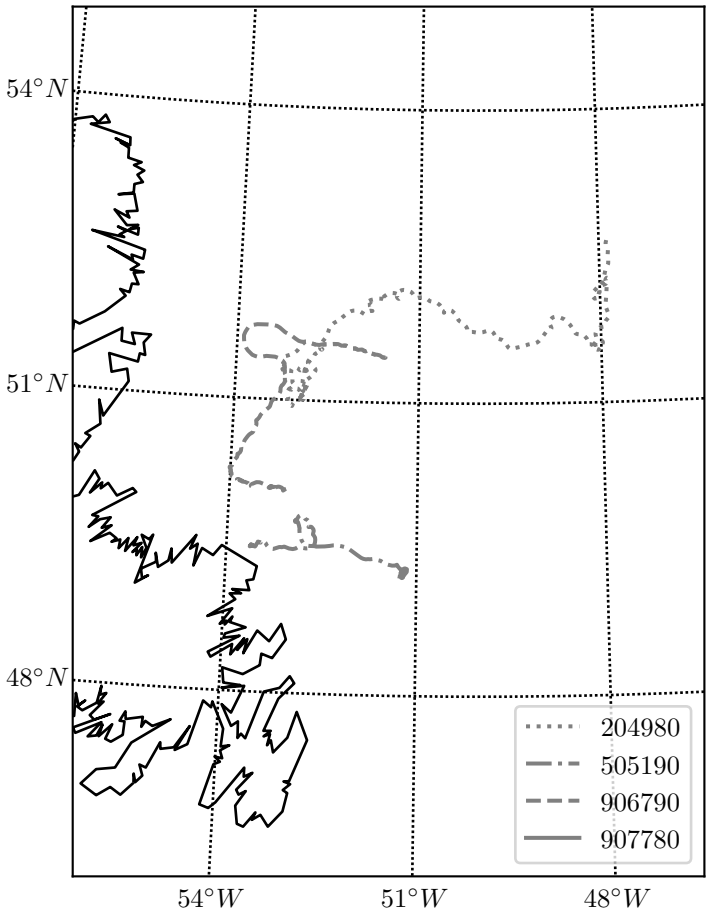

Figure 4.8: All data on the location of iceberg's transmitted by the beacons 204980, 505190, 906790, and 907780 that were deployed during the Statoil-ArcticNet research expedition of 2015.

Figure 4.9: An iceberg monitored during the Statoil-ArcticNet Research Expedition of 2015. Attached to the iceberg are two beacons with identification numbers 204980 and 906790. Source: (Polar Data Catalogue, 2015).

Figure 4.10: An iceberg monitored during the Statoil-ArcticNet Research Expedition of 2015. Attached to the iceberg are two beacons with identification numbers 505190 and 907780. Source: (Polar Data Catalogue, 2015).

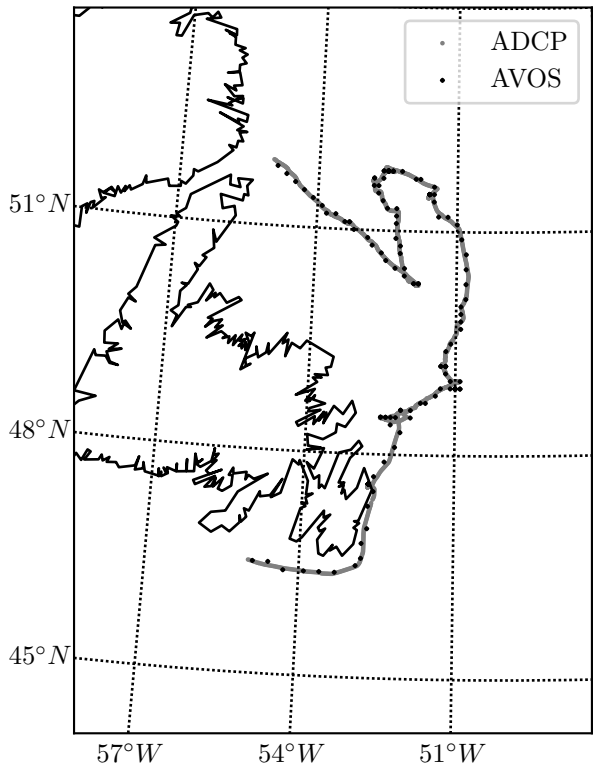

Figure 4.11: Locations of observations made by the ADCP and AVOS devices onboard the CCGS Amundsen. ADCP and AVOS measurements were taken roughly every 5 minutes and 60 minutes, respectively.

In order to get observational metocean data that could be compared to the model metocean data used in running drift simulations of these icebergs, we focused on a subset of data that was near the icebergs in time and space. The observational measurements in this subset can be seen in Figure 4.11.

4.2.2 ADCP

An Acoustic Doppler Current Profiler (ADCP) is a hydroacoustic device used to measure ocean current velocity at depth. ADCP devices work by transmitting and

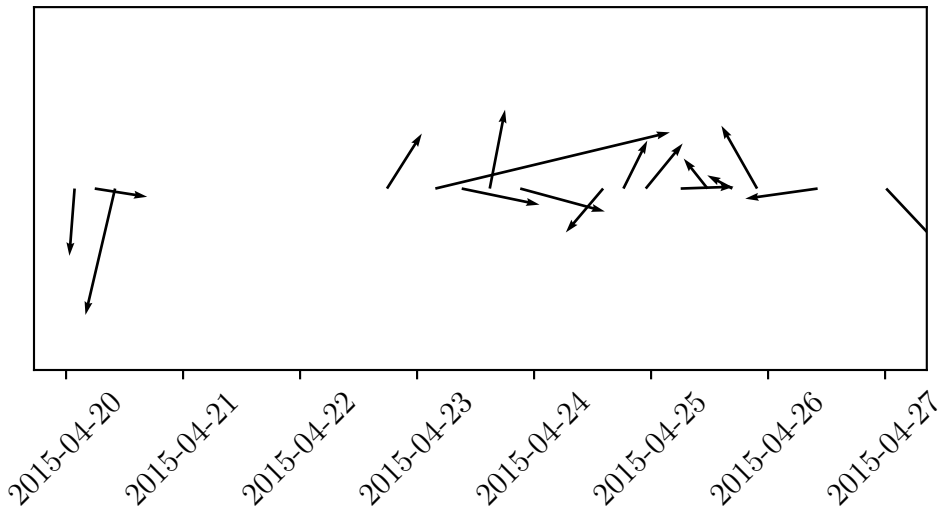

Figure 4.12: Ocean current velocity measured by an ADCP over time at a depth of roughly 23 m. The quiver arrows plotted are spaced evenly with one arrow for every 4 hours for clarity purposes. The spaces where an arrow is missing at one of these 4 hour intervals is due to the absence of a valid measurement at that point in time.

receiving sound waves, then calculating the travelling time of the waves to estimate the distance, and measuring the frequency of the echo to obtain the current velocity.

The ADCP data was collected by a vessel-mounted Ocean Surveyor (RDI 150 kHz) at 45 depth levels from 23.19 – 375.17 m. Figure 4.12 shows a subset of the current velocities measured over a week-long time frame.

4.2.3 AVOS

The CCGS Amundsen is equipped with an Environment Canada Automatic Voluntary Observing Ship system (AVOS) that contains several devices for recording data continuously for a number of quantities (AVOS DATA Processing Notes, 2015).

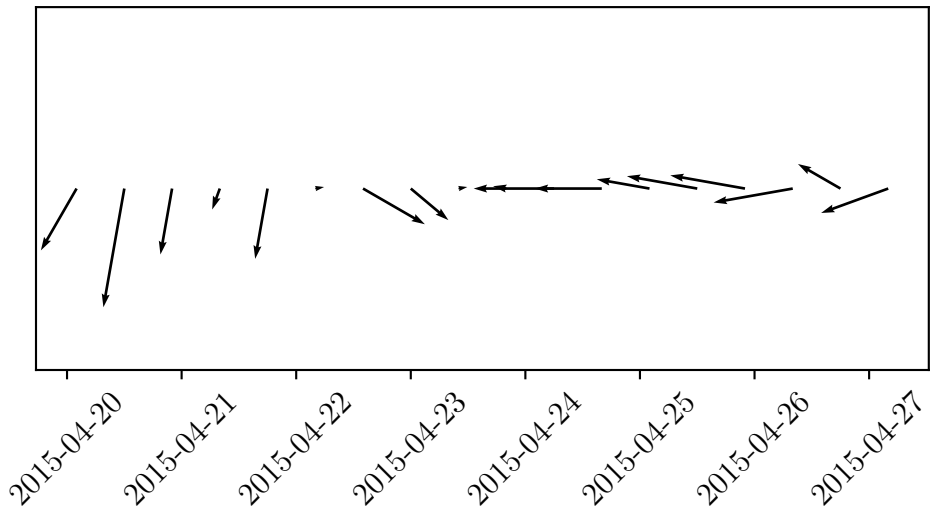

Figure 4.13: Quiver arrows for the true wind velocity measured by the AVOS aboard the Amundsen at roughly 10 m. The arrows plotted are spaced evenly with one arrow for every 8 hours for clarity purposes.

Among these is the Young R.M. Anemometer which is used for measuring apparent wind speed and direction. The range and accuracy for apparent wind speed are 0 to 100 m/s and 0.3 m/s, respectively, and the range and accuracy for apparent wind direction are 0 to 360 degrees and 3 degrees, respectively. Sensors are placed at 21.6 m above the waterline and 5.5 m above the wheelhouse roof. In post-processing, the true wind is calculated by taking into account the ship's speed and heading from the data collected by the ship's gyrocompass. The raw data time series (1 Hz) is then averaged into an hourly time series. The final data uncertainty for wind speed and direction are then ± 1 knt and $\pm\ 5^{\circ}$, respectively. Figure 4.13 shows a subset of the wind velocities measured over a week-long time frame.

4.2.4 Comparing Observational Data to Model Data

In order to get an assessment of the accuracy of the model current and wind velocities used in the simulations in this work, it was assumed that the current and wind velocities measured by the ADCP and AVOS devices aboard the Amundsen were close to the true values. With this assumption in mind, the model data was then interpolated to the precise location of the device measurements recorded. The comparisons between observed and model current and wind velocities are seen in Figures 4.14 and 4.15. Observe that the agreement between the measured and model values, especially in the case of the ADCP, is not always close. This suggests that there exists random variability that can't be predicted by interpolating pointwise values.

Once the model velocity is interpolated to the appropriate time and space of the observational measurements, the difference between the model and observed velocities can then be taken and a distribution of corrections can be made. Since there are two components to current and wind velocities (Eastward and Northward), a bivariate distribution can be used. This would be preferential to having two univariate distributions of corrections (magnitude and direction) for each velocity field because it is likely that the two components are correlated. The bivariate distributions chosen for both the current and wind velocity corrections are bivariate normal (seen in Figures 4.16 and 4.17).

These distributions are important because they are used later in doing ensemble iceberg drift simulations with data for the icebergs studied during the Statoil-ArcticNet research expedition of 2015.

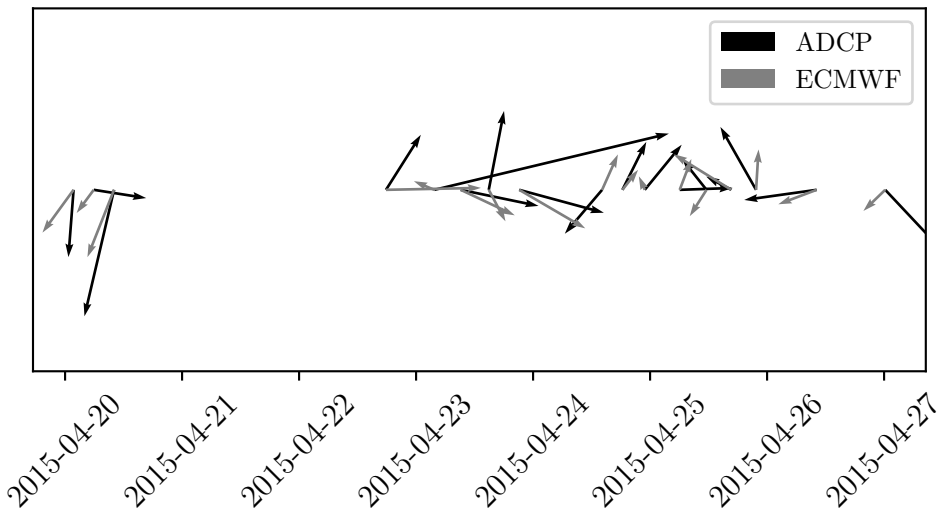

Figure 4.14: Quiver arrows for the current velocities measured by the ADCP device aboard the Amundsen and the current velocities from the ECMWF ocean model used (see Section 2.2.2). The large gap between arrows between roughly 2015-04-20 and 2015-04-23 is due to missing data points from the ADCP device. The observed and model data is for depths of roughly 23 and 0.5 m, respectively.

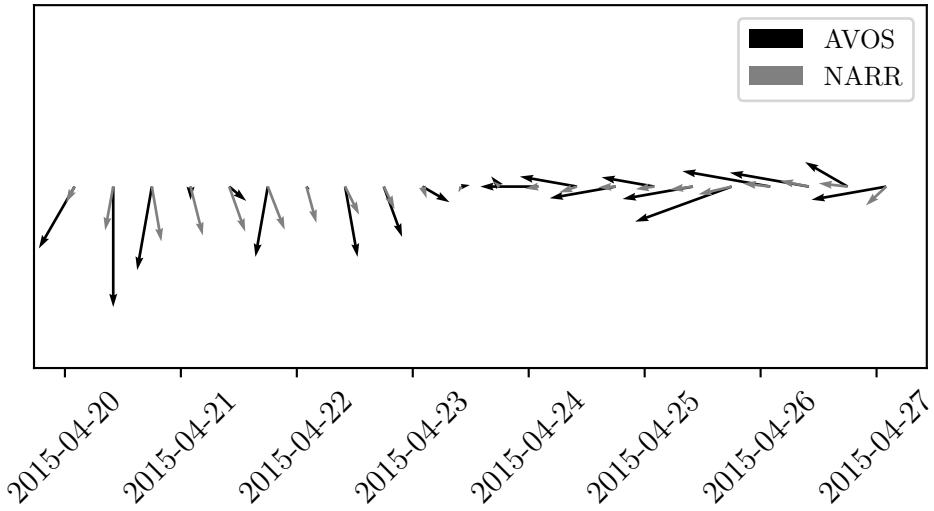

Figure 4.15: Quiver arrows for the wind velocities measured by the AVOS device aboard the Amundsen and the wind velocities from the NARR atmospheric model used (see Section 2.3.1). The observed and model data are both for heights of roughly 10m.

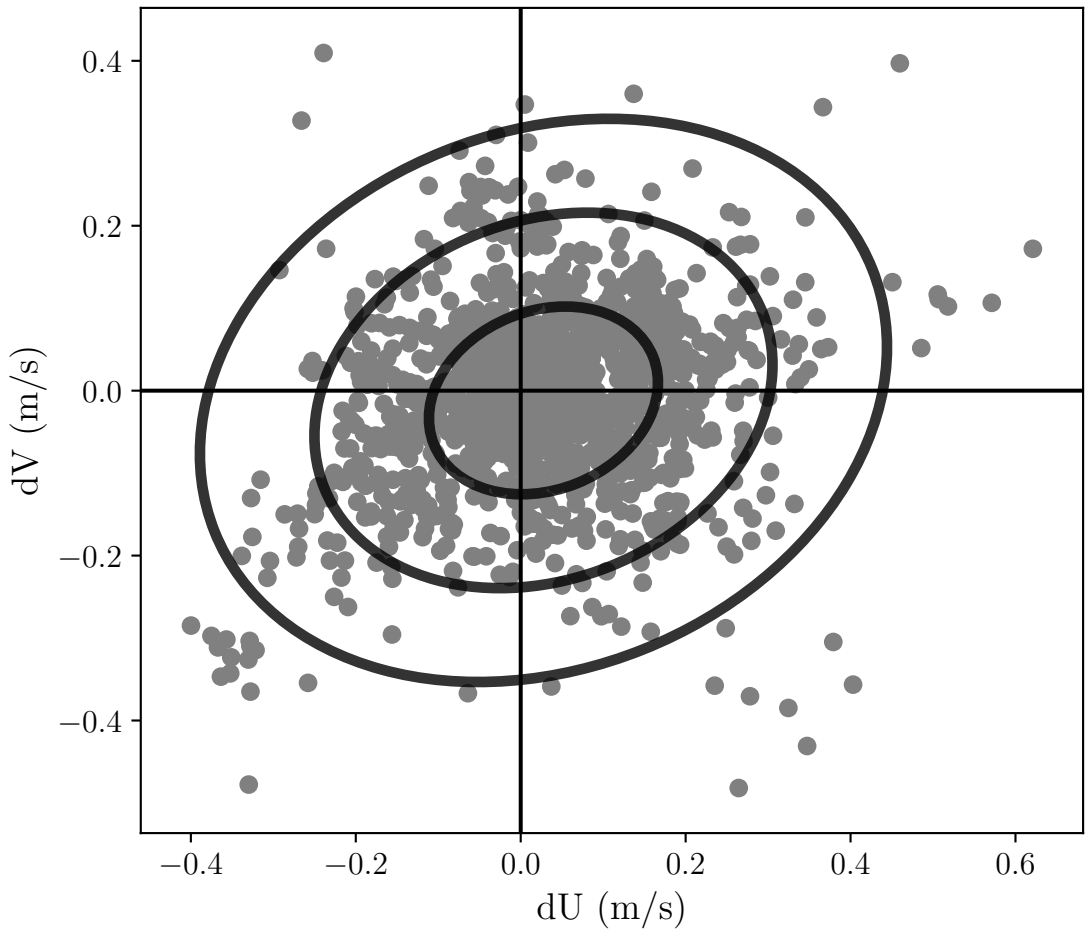

Figure 4.16: Bivariate normal distribution of current velocity corrections with the data being the component-wise difference between the ADCP and ECMWF current velocity data sets. The mean of this distribution is (0.028, -0.012), the standard deviation is (0.14, 0.11), and the rotation counter-clockwise about the origin is 0.38. The ellipses represent first three standard deviations of the distribution.

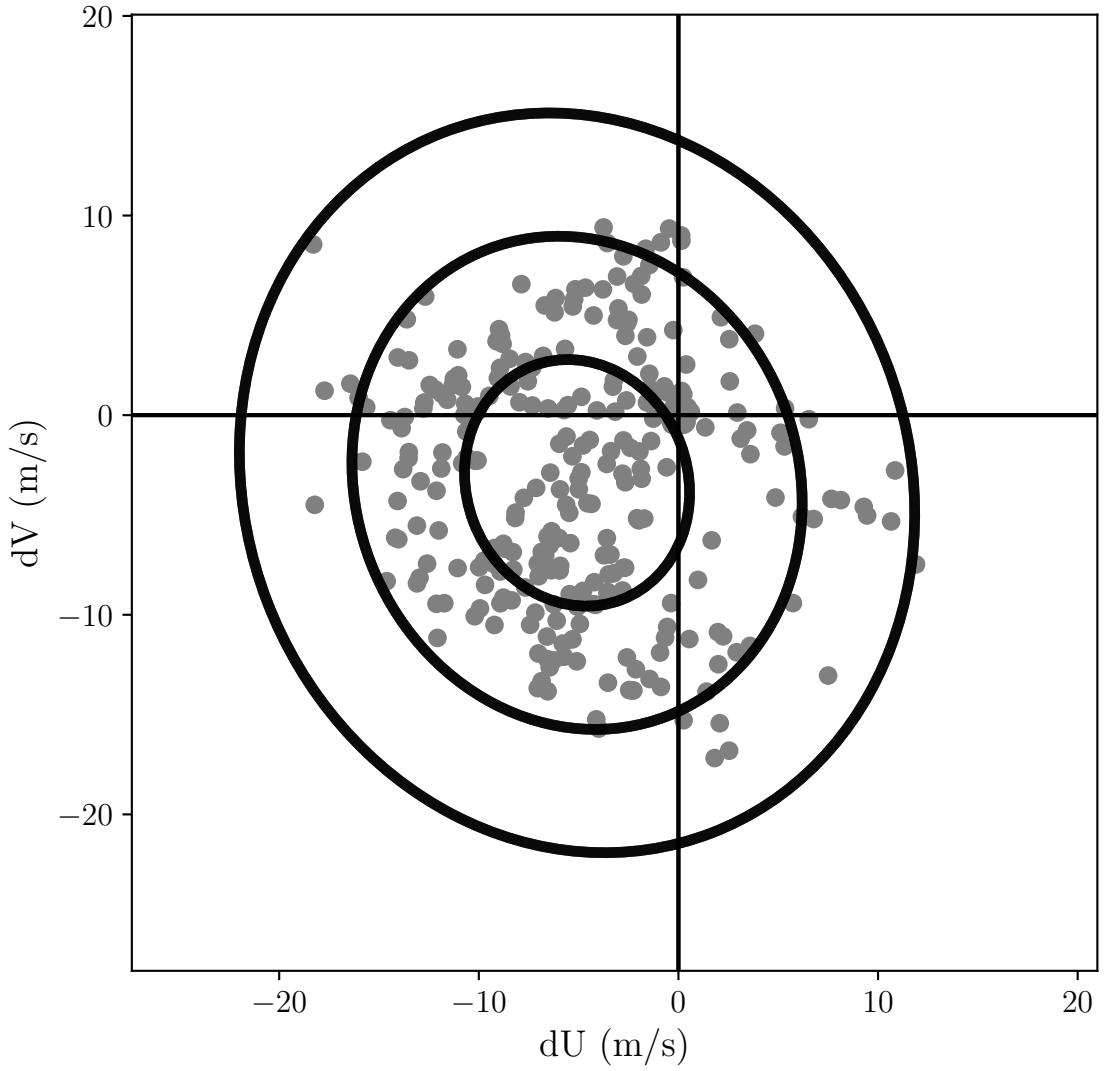

Figure 4.17: Bivariate normal distribution of wind velocity corrections with the data being the component-wise difference between the AVOS and NARR wind velocity data sets. The mean of this distribution is (-5.1, -3.4), the standard deviation is (6.3, 5.5), and the rotation counter-clockwise about the origin is -1.2. The ellipses represent the first three standard deviations of the distribution.

4.3 Ensembles

In *ensemble forecasting*, multiple simulations are created to account for uncertainties that come from errors in the initial conditions and the errors in the model itself and/or the numerical methods used to solve the equations. For iceberg drift forecasting, these uncertainties are inherent in the starting location and velocity of the iceberg, the physical iceberg properties (such as the geometry, density, and drag coefficients), the wind and ocean current velocities, the equations of motion that depict the physics of iceberg drift, and the numerical methods used to solve these equations. Since the Statoil-ArcticNet research expedition of 2015 collected data on iceberg drift and current and wind velocities, this gives us iceberg drift tracks to use as a reference (which inherently also gives us an initial iceberg velocity) and allows us to use the wind and current measurements to create distributions of corrections (see Section 4.2), which can be used to perturb the model wind and current velocities used in the iceberg drift simulations.

This approach, however, has one major flaw and that is that the observed current and wind velocity data collected contains just the observations from one location at each step in time. Furthermore, this location is constantly changing since the vessel that houses the ADCP and AVOS devices used for taking these observational measurements is moving. Nonetheless, the distributions of corrections created in Section 4.2 are used to perturb the wind and current velocities in the following way: at each time step in the iceberg drift simulation, the wind and current velocities used as inputs in the drift model are given by

$$\mathbf{V}^i = \mathbf{V}^i_m + s^{i-1}(1-\alpha) + s^i\alpha \tag{4.1}$$

where $i = 1, 2, \ldots n$ is the time step, $\mathbf{V^i}$ is the velocity used in the drift model, $\mathbf{V}^i_m$ is the velocity obtained from the model by interpolating the model data to the current iceberg position at time t^i, s^i is the sample drawn from the distribution of corrections at time step i, and $\alpha \in [0, 1]$ is a constant that affects the noisiness of the value of $\mathbf{V^i}$ by affecting the persistence of the samples at previous time steps in the current one.

Our results show that this approach worked well sometimes and poorly at other times for each iceberg. We will now look at one example where the ensemble cone encapsulated most of the observed iceberg track and one where it did not. We will also compare this approach to the traditional method of deterministic forecasting (without perturbing the wind and current velocities using the distributions of corrections).

4.3.1 Case Study: Iceberg Trajectory with a Good Fit

The drift track we will now look at comes from the transmitted data of the beacon with identification number 906790. This iceberg is described in terms of its shape only as a "saddle" shaped iceberg, a shape for which we have no corresponding information (see Table 2.2 for known shape classes), therefore, it was assumed to be tabular (TAB). There is also no size information provided, so it was assumed to be within the large (LG) size class (see Table 2.1). The time period of interest for this iceberg is the approximate 24-hour period between April 24th 21:54:40 and 25th 21:52:09, 2015. The drift track for this time is shown in Figures 4.18 and 4.19.

Here we can see that the iceberg travelled approximately 13 km towards the

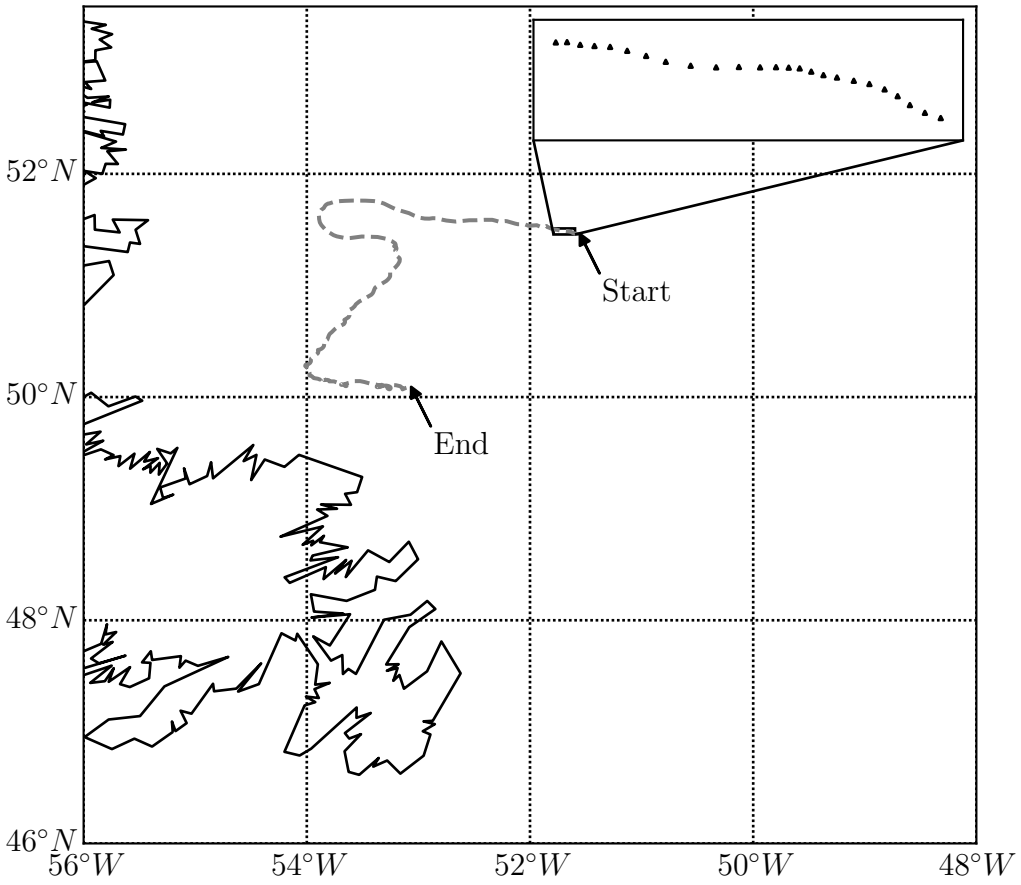

Figure 4.18: Iceberg drift track obtained from beacon 906790 deployed during the Statoil-ArcticNet research expedition of 2015. The area enclosed in the inset map shows the points indicating the location of the iceberg during the period between April 24th 21:54:40 and 25th 21:52:09, 2015.

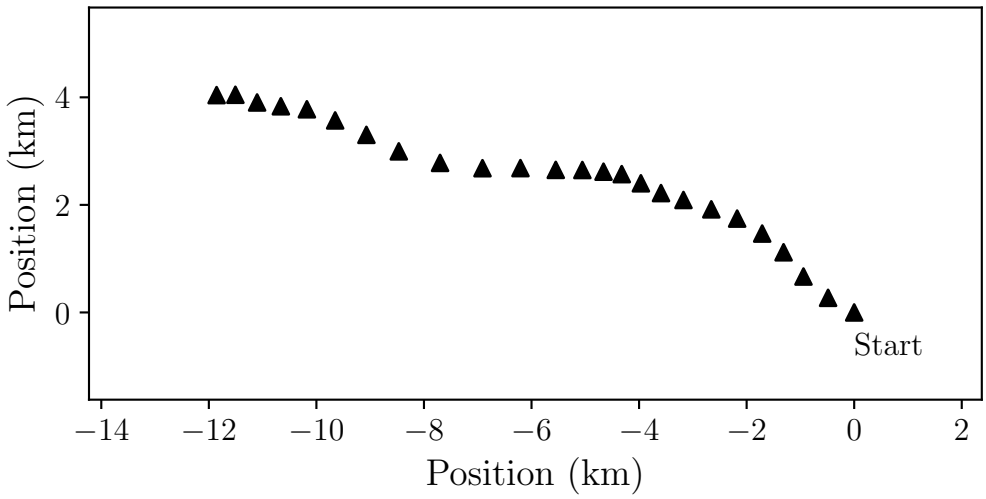

Figure 4.19: Relative movement of the iceberg during the period between April 24th 21:54:40 and 25th 21:52:09, 2015 (obtained from beacon 906790 deployed during the Statoil-ArcticNet research expedition of 2015).

Northwest. The velocity during this time period was not constant, but varied between approximately 0.1 and 0.22 m/s (see Figure 4.20).

The wind velocity data around the iceberg's location for this time period (seen in Figure 4.21) shows that the wind speed and direction varied slightly (between approximately 5 – 7 m/s blowing from the Northeast – Southeast, respectively).

The current velocity data around the iceberg's location for this time period (seen in Figure 4.22) shows that the current speed and direction varied slightly (between approximately 0.1 – 0.2 m/s flowing towards between Northwest and Northeast).

In order to run a drift simulation, values of C_a and C_w must be chosen. Since there does not seem to be any consensus in the literature on what those values are (see Section 2.1), we ran simulations with values linearly spaced between 0.5 and 2.5 for each (Allison et al., 2014) (see Section 2.1.2.1 for justification), as shown in Figure

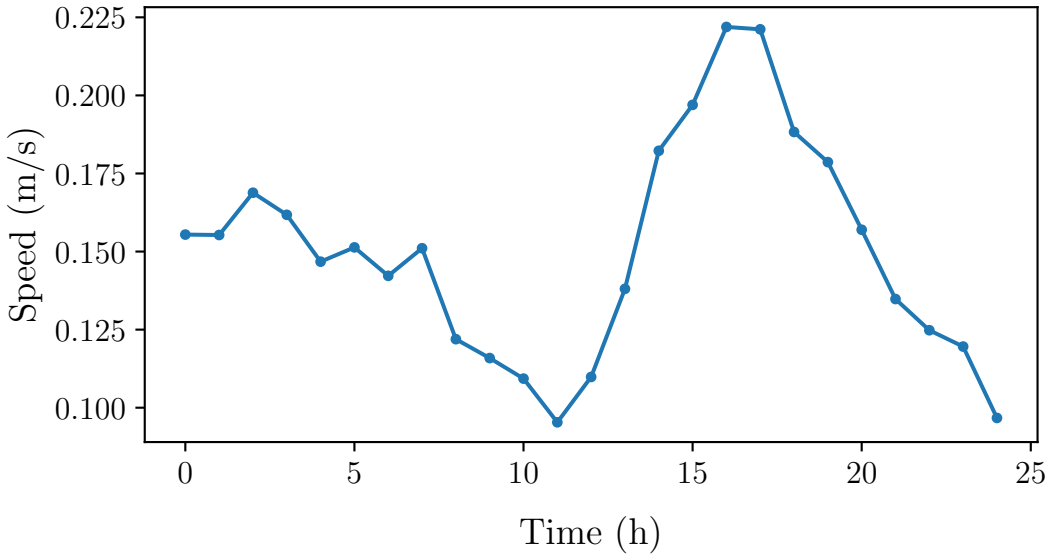

Figure 4.20: Iceberg speed during the period between April 24th 21:54:40 and 25th 21:52:09, 2015 (obtained from beacon 906790 deployed during the Statoil-ArcticNet research expedition of 2015).

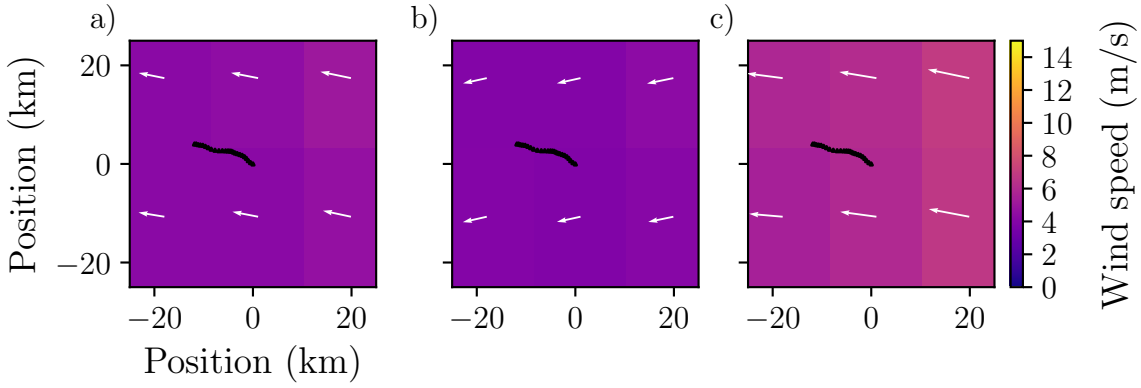

Figure 4.21: Wind velocity data from the NARR atmospheric model. Subplots a), b), and c) show a snapshot of the wind velocity at 0, 12, and 24 hours from the start of the simulation. The observed iceberg drift track is also included in each of the subplots for reference.

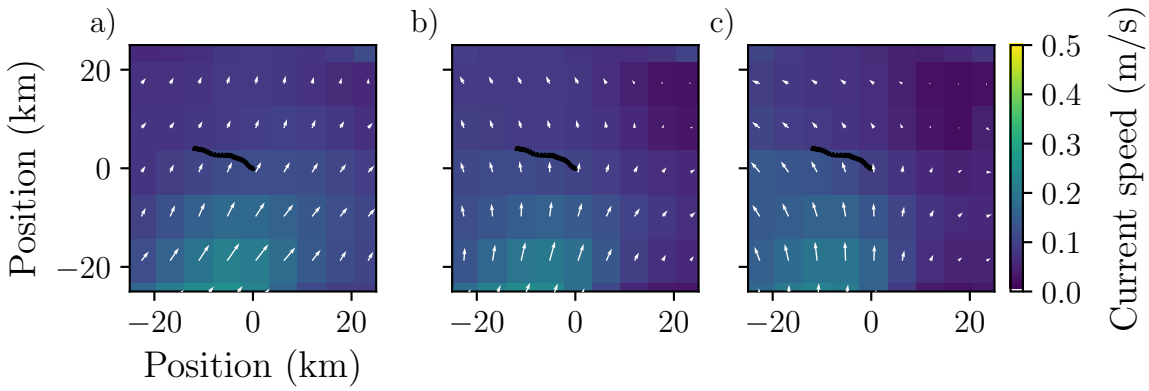

Figure 4.22: Current velocity data from the ECMWF ocean model. Subplots a), b), and c) show a snapshot of the current velocity at 0, 12, and 24 hours from the start of the simulation. The observed iceberg drift track is also included in each of the subplots for reference.

4.23.

Each simulated track was then compared to the observed drift track by interpolating their position at each point in time along the observed track. These values were then used to compute the root mean square error (RMSE) using the equation

$$\epsilon = \sqrt{\frac{\sum_{i=1}^{n}(x_i^* - x_i)^2 + (y_i^* - y_i)^2}{n}}, \tag{4.2}$$

where x^*, y^* and x, y are the positions of the observed and simulated iceberg, respectively, i is the index that represents a point in time, and n is the total number of points in time for which we have data. After calculating the RMSE for each simulated drift track, we then chose the values of C_a and C_w that corresponded to the drift track with the lowest RMSE (see Figure 4.24) to be used in the ensemble.

For this particular ensemble, a value of 1.0 was chosen for both C_a and C_w.

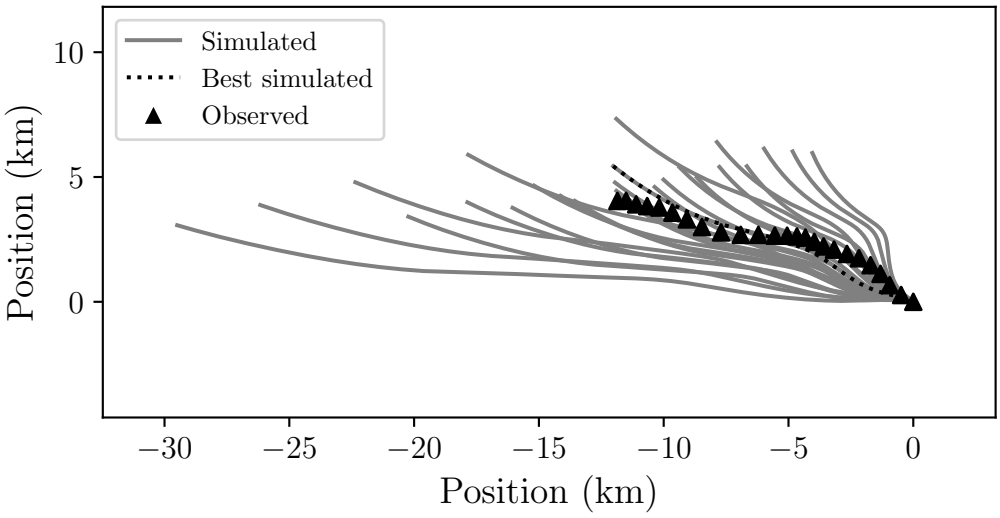

Figure 4.23: Iceberg drift simulations with various values of C_a and C_w. Each simulated run was evaluated for its agreement with the observed iceberg track based upon the root mean square error (RMSE) between the simulated run and the observed iceberg track.

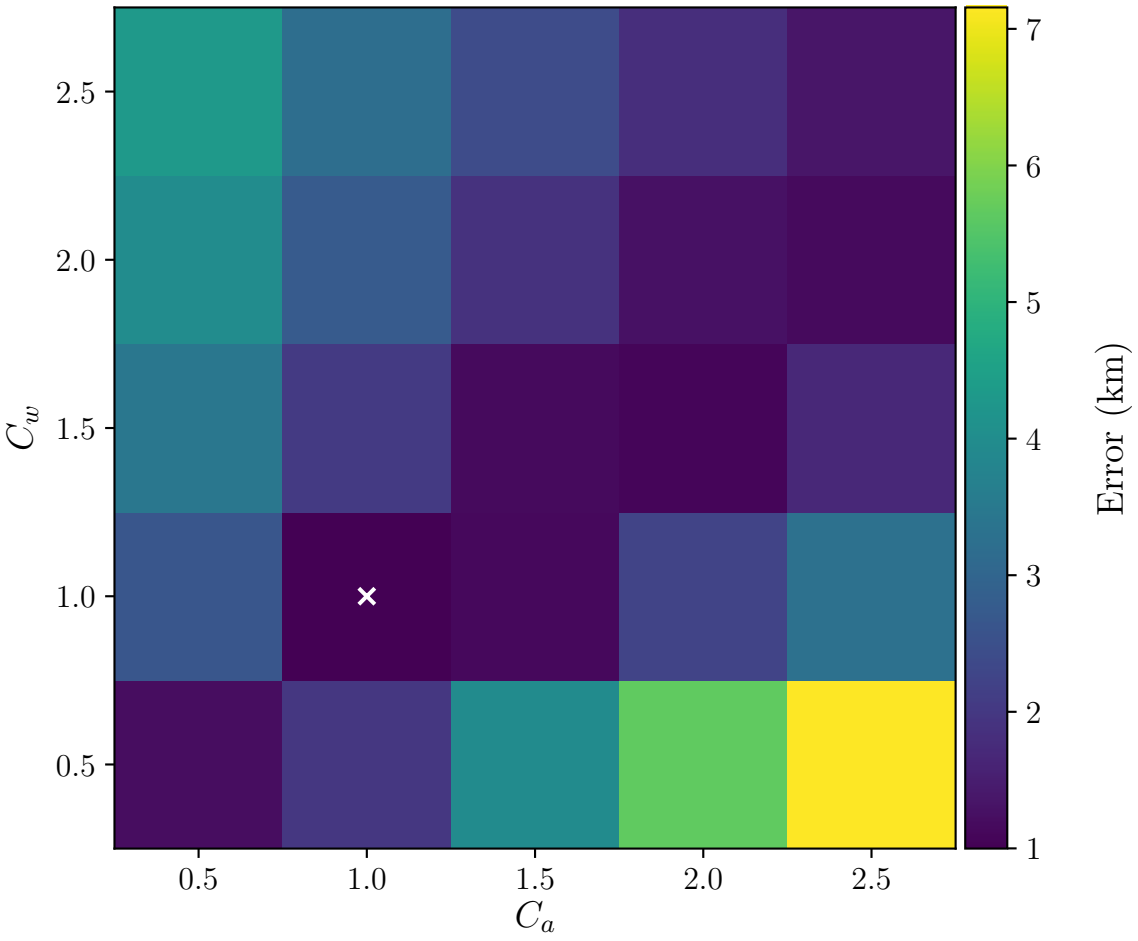

Figure 4.24: The error associated with the runs simulated with various values of C_a and C_w. The error is the root mean square error (RMSE) between the simulated track and the observed track (see Equation 4.2).

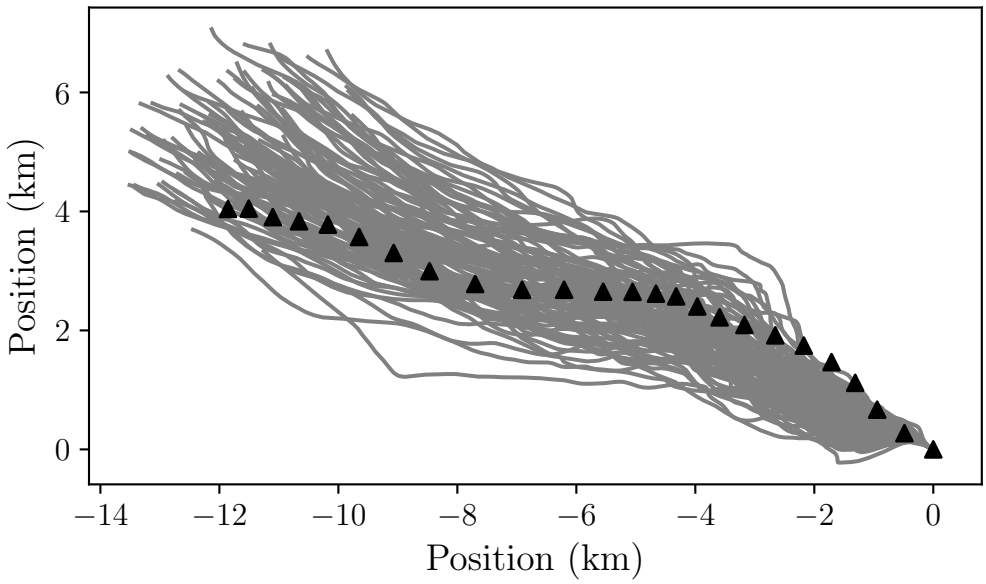

Figure 4.25: Ensemble of simulations performed by perturbing winds and currents by sampling from their determined distributions.

Therefore, the fixed inputs that went into the model were the iceberg's start velocity (calculated by taking the rate of change between the first two observed points), the iceberg's starting location (the location of the first observed point in time), the start time (the observed iceberg's first point in time), the end time (the observed iceberg's last point in time), and the values of C_a and C_w calculated to have the lowest RMSE for this track.

Using these fixed inputs, the ECMWF ocean model, the NARR atmospheric model, and the correction distributions to perturb the model velocities, a 100 member ensemble was simulated and compared to the observed iceberg's drift track, see Figure 4.25.

As can be seen from the"spaghetti plot" in Figure 4.25, the spread of the ensemble

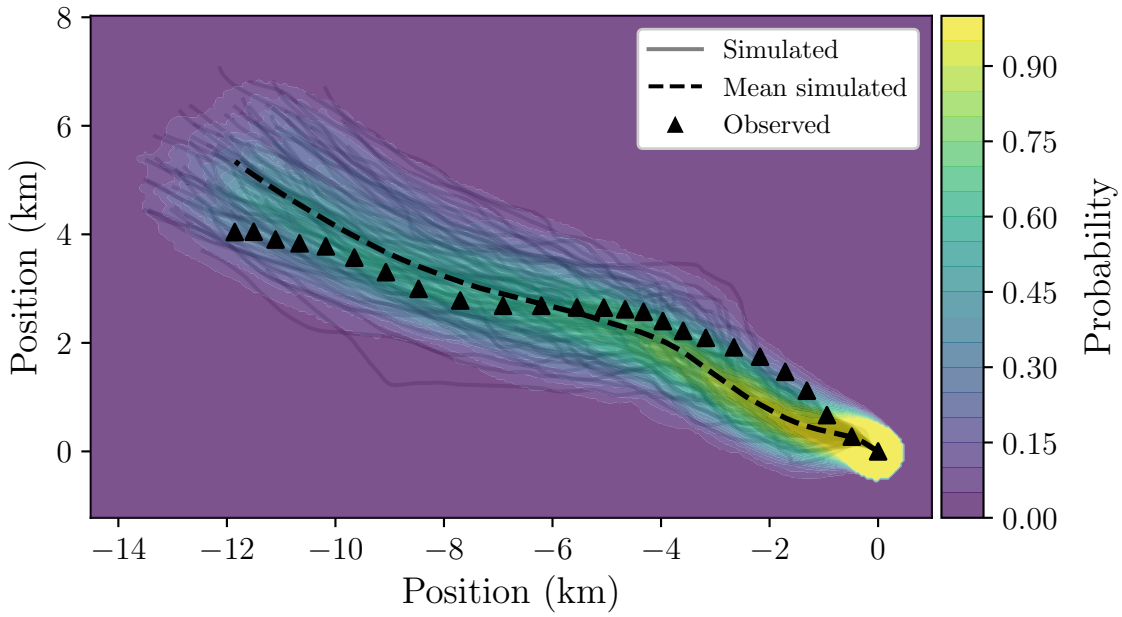

Figure 4.26: Probability of finding an iceberg which contained beacon 906790 deployed during the Statoil-ArcticNet research expedition of 2015 at any given location during the time span of the period between April 24th 21:54:40 and 25th 21:52:09, 2015 based on the results of an ensemble drift prediction (with a radius set to 0.5 km).

is not large (approximately between 20 – 40°) and most of the observed iceberg's location points were overlapped by one or more members of the ensemble. From this information, the probability of finding an iceberg at any given point in space can be estimated, see Figure 4.26.

This plot (Figure 4.26), was created by assigning a value of 1 to each of the grid cells within a radius of 0.5 km of each of the points in each of the ensemble members and then dividing by the total number of members. The reason why a radius of 0.5 km was chosen is because that is approximately the radius of the "Ice Exclusion Area" (the area within the red circle) in Husky's Emergency Management Plan (refer

to Figure 1.1).

By inspection, this plot shows that the probability of finding any given point in the observed iceberg's track within the spread of the ensemble is greater than 0. This is supported by Figure 4.27. Furthermore, if we look at the RMSE over time (Figure 4.28), we can see that the maximum RMSE never exceeds 2 km. It should also be noted that the shape of the ensemble forecast also resembles the shape of the observed track.

If we then compare these results to their deterministic counterpart, we find that we cannot encapsulate the observed drift track with any realistic values of C_a and C_w (see Figures 4.29, 4.30, and 4.31).

4.3.2 Case Study: Iceberg Trajectory with a Bad Fit

The drift track we will now look at comes from the transmitted data of the beacon with identification number 505190. This iceberg is described in terms of its shape as tabular (TAB) (see Table 2.2), however, there is no size information provided, so it is assumed to be within the large (LG) size class (see Table 2.1). The time period of interest for this iceberg is the approximate 24-hour period between April 23rd 23:59:26 and 25th 00:58:13, 2015. The drift track for this time is shown in Figures 4.32 and 4.33. Here we can see that the iceberg travelled approximately 12 km towards the Northeast. The velocity during this time period was not constant, it varied between approximately 0.05 and 0.25 m/s (see Figure 4.34).

The wind velocity data around the iceberg's location for this time period (seen in Figure 4.35) shows that the wind speed and direction varied greatly (between

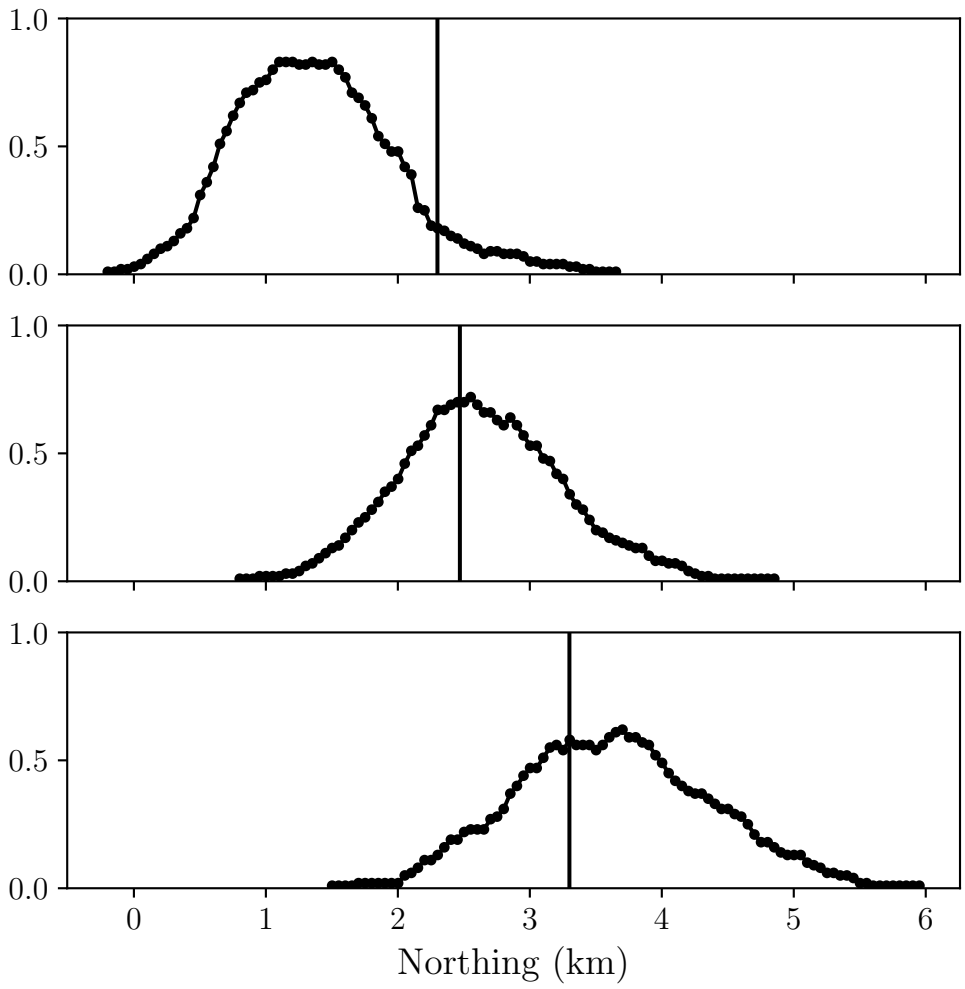

Figure 4.27: The probability distribution of the ensemble iceberg forecast as a function of the Northing coordinate at fixed values for the Easting coordinate. The upper, middle, and lower plots are at fixed Easting's of -3, -6, and -9 km East from the starting position. The vertical line represents the actual Northing of the observed iceberg.

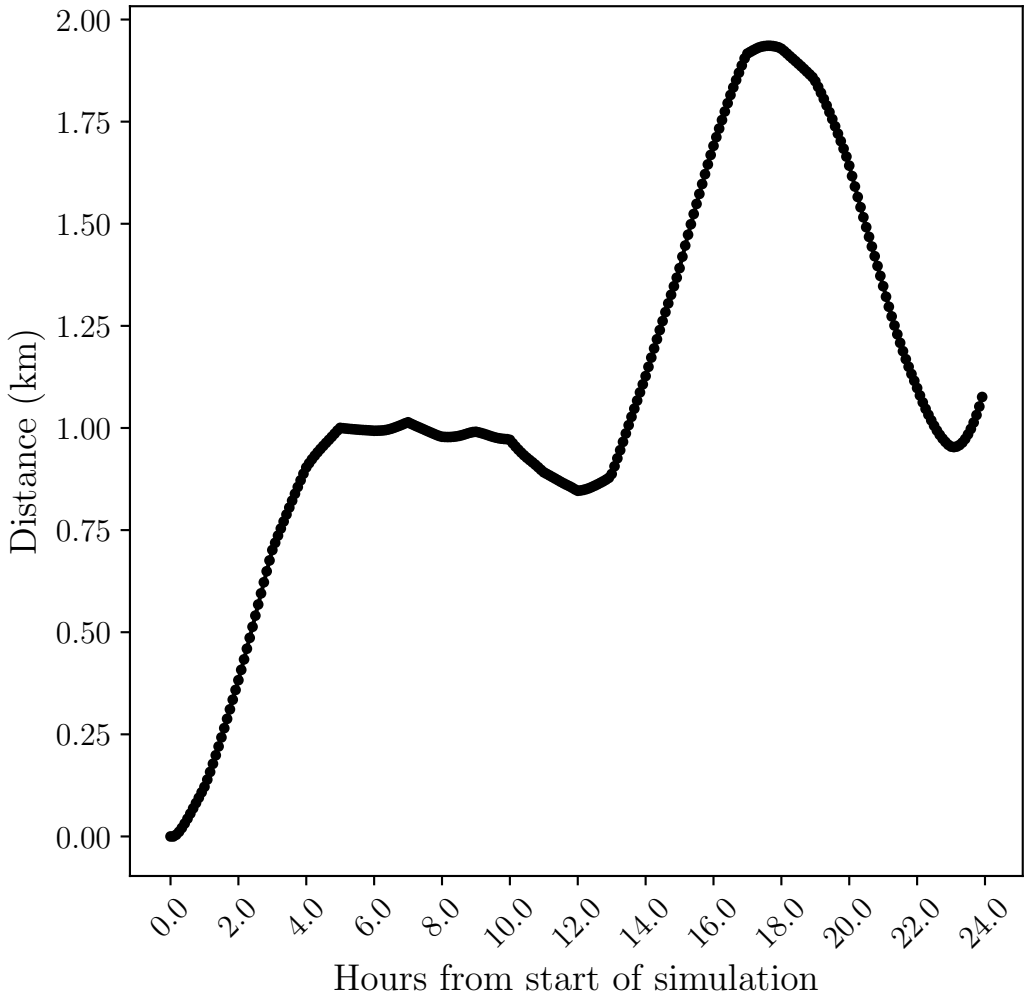

Figure 4.28: The RMSE (km) of the mean of the ensemble forecast over time to the actual position of the observed iceberg over time.

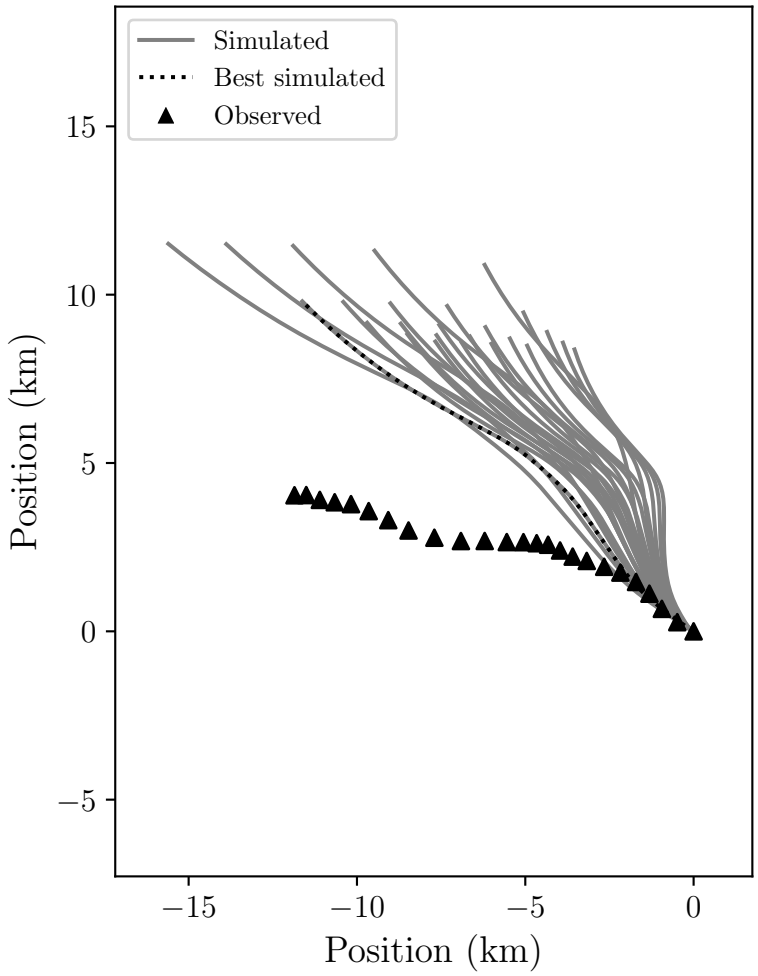

Figure 4.29: Iceberg drift simulations with various values of C_a and C_w and the means of the current and wind correction distributions added to the current and wind velocities; respectively. Each simulated run was evaluated for its agreement with the observed iceberg track based upon the root mean square error (RMSE) between the simulated run and the observed iceberg track.

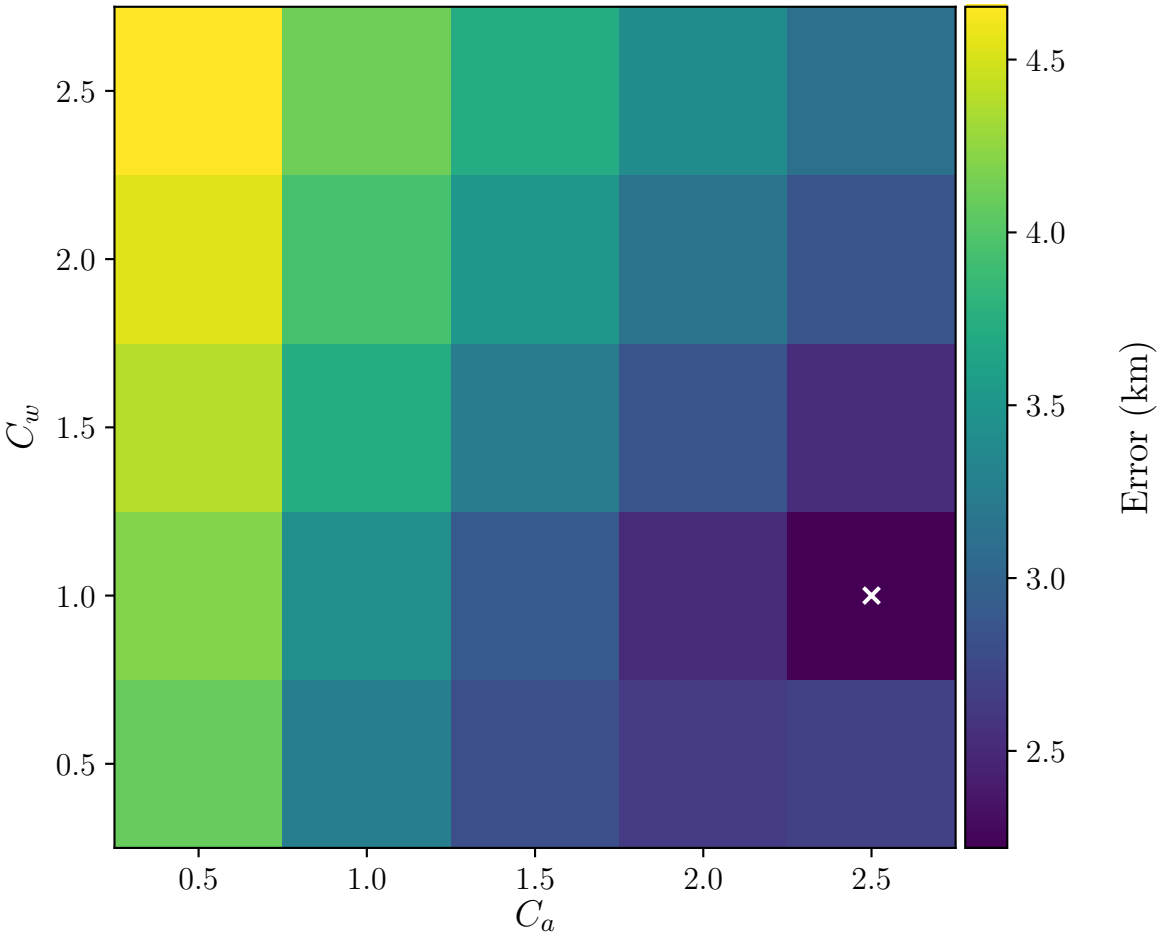

Figure 4.30: The error associated with the runs simulated with various values of C_a and C_w and the means of the current and wind correction distributions added to the current and wind velocities; respectively. The error is the root mean square error (RMSE) between the simulated track and the observed track (see Equation 4.2).

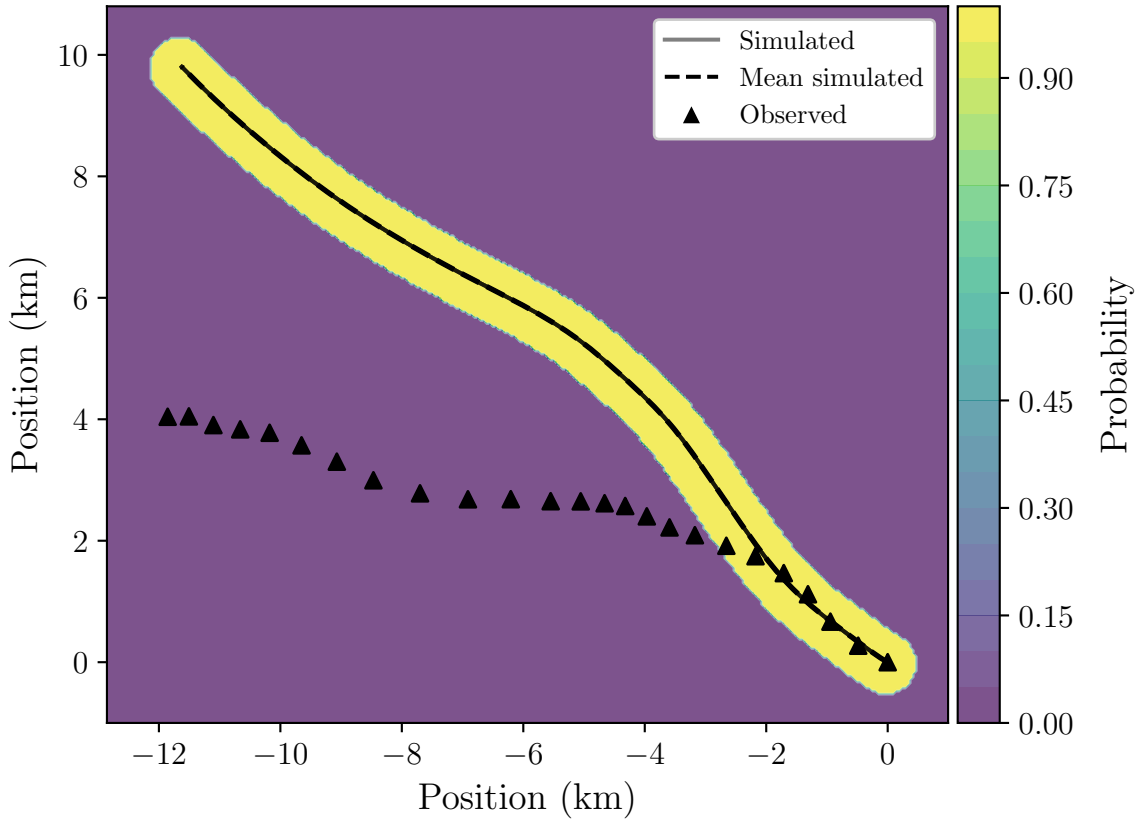

Figure 4.31: Probability of finding an iceberg which contained beacon 906790 deployed during the Statoil-ArcticNet research expedition of 2015 at any given location during the time span of the period between April 24th 21:54:40 and 25th 21:52:09, 2015 based on the results of a single deterministic drift prediction (with a radius set to 0.5 km).

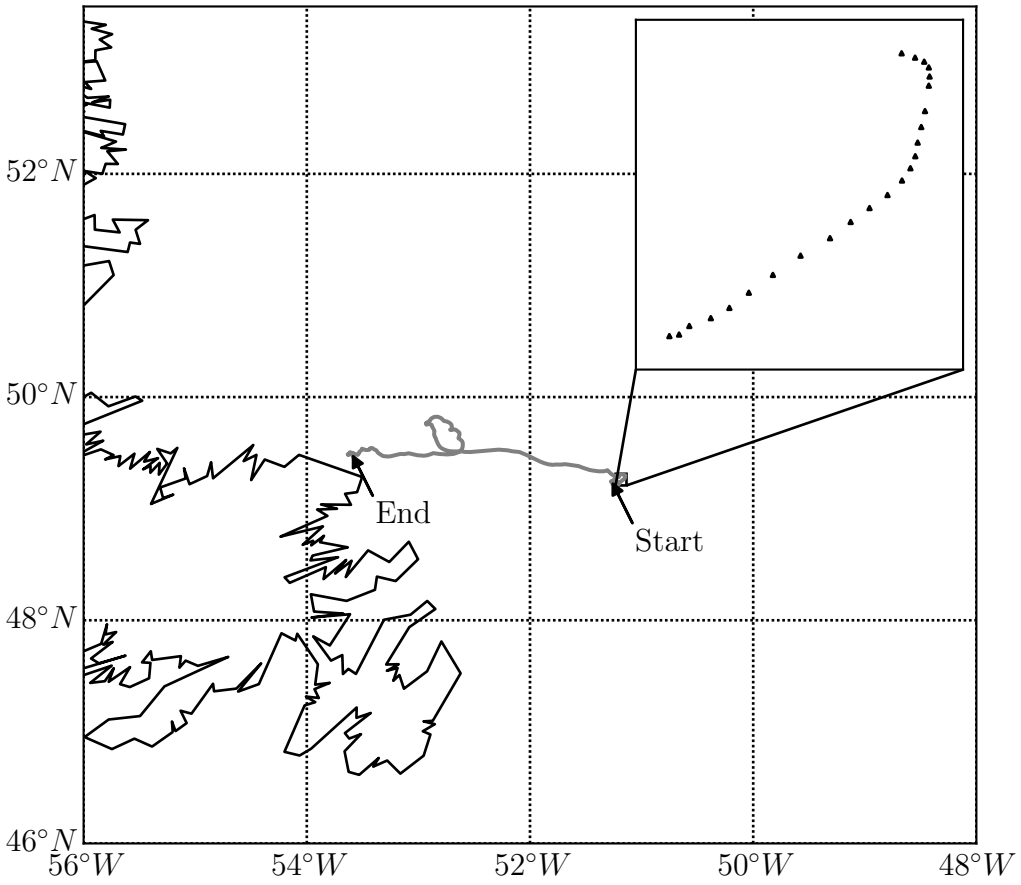

Figure 4.32: Iceberg drift track obtained from beacon 505190 deployed during the Statoil-ArcticNet research expedition of 2015. The area enclosed in the inset map shows the points indicating the location of the iceberg during the period between April 23rd 23:59:26 and 25th 00:58:13, 2015.

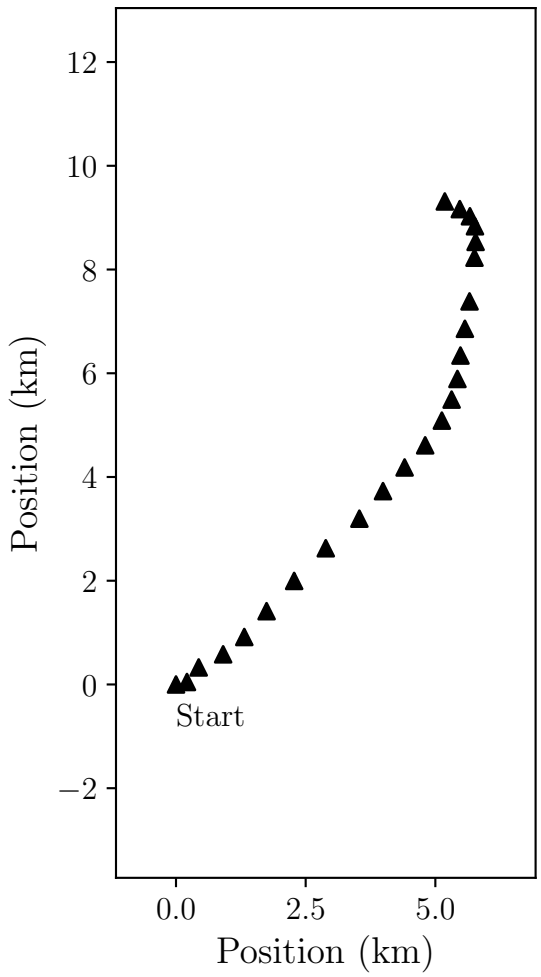

Figure 4.33: Relative movement of the iceberg during the period between April 23rd 23:59:26 and 25th 00:58:13, 2015 (obtained from beacon 505190 deployed during the Statoil-ArcticNet research expedition of 2015).

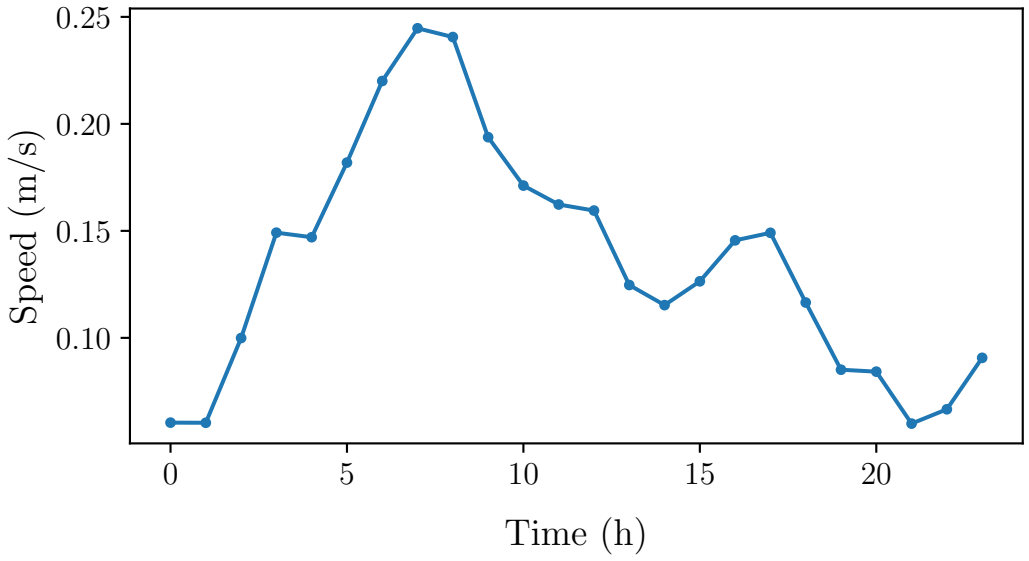

Figure 4.34: Iceberg speed during the period between April 23rd 23:59:26 and 25th 00:58:13, 2015 (obtained from beacon 505190 deployed during the Statoil-ArcticNet research expedition of 2015).

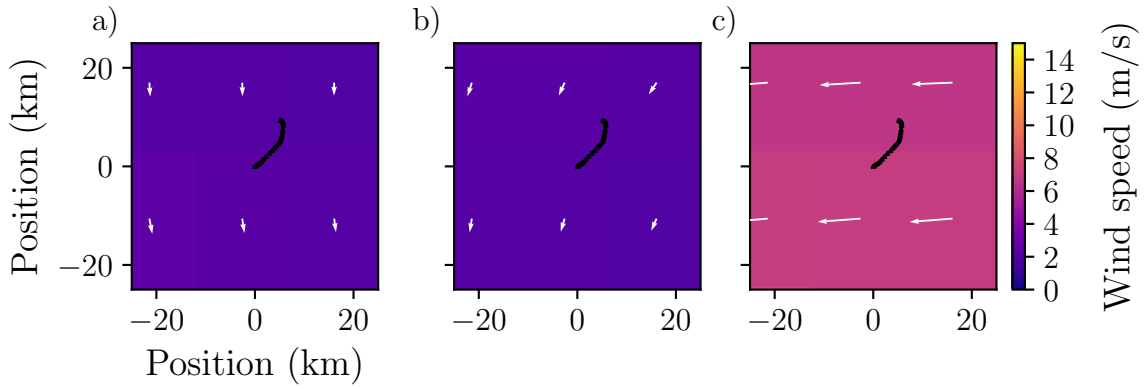

Figure 4.35: Wind velocity data from the ECMWF ocean model. Subplots a), b), and c) show a snapshot of the current velocity at 0, 12, and 24 hours from the start of the simulation. The observed iceberg drift track is also included in each of the subplots for reference.

approximately 0 – 8 m/s blowing from between the South and East, respectively). Note that, in this case, the velocity of the iceberg does not correlate well with the velocity of the wind.

The current velocity data around the iceberg's location for this time period (seen in Figure 4.36) shows that the current speed and direction varied greatly (between approximately 0 – 0.3 m/s flowing in a wide range of different directions).

It is suspected that part of the reason why this ensemble does a poor job of enveloping the observed iceberg's location points is because the current field around the iceberg at the time of this simulation has a high divergence. This means that at any given time, a slight shift in the location of the nodes on the current field's grid could cause a large change to the trajectory of the simulated iceberg.

As above, we first searched the parameter space of C_a and C_w to find optimal

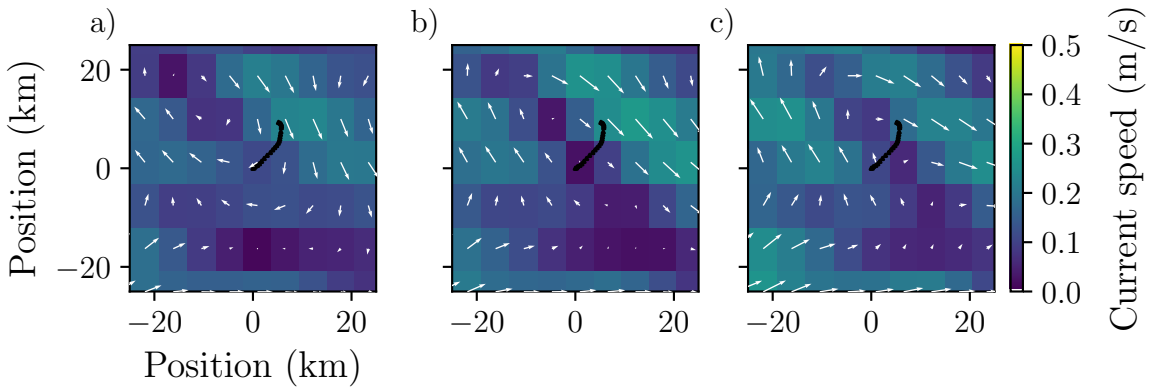

Figure 4.36: Current velocity data from the ECMWF ocean model. Subplots a), b), and c) show a snapshot of the current velocity at 0, 12, and 24 hours from the start of the simulation. The observed iceberg drift track is also included in each of the subplots for reference.

values for them based upon their RMSE. This time, however, all combinations of C_a and C_w returned a high value for the RMSE (see Figures 4.37 and 4.38).

The results of this optimization found that the RMSE is lowest when C_a is 0.5 and C_w is 2.5; here, the RMSE is approximately 9 km (a much greater value than the value of approximately 2 km for the example above considering that the distances travelled by each of the two icebergs is approximately the same). Notice, too, that these values lie in the corner of the parameter space considered. This is concerning, but there is little in the literature that supports extending the bounds above or below these values, so these values were chosen and the ensemble was run.

The result of this ensemble (seen in Figures 4.39 and 4.40) shows a reasonable ensemble spread of about 10 – 30°; however, almost all of the observed iceberg's location points lie in the 0 probability region. This reflects poorly upon the ability

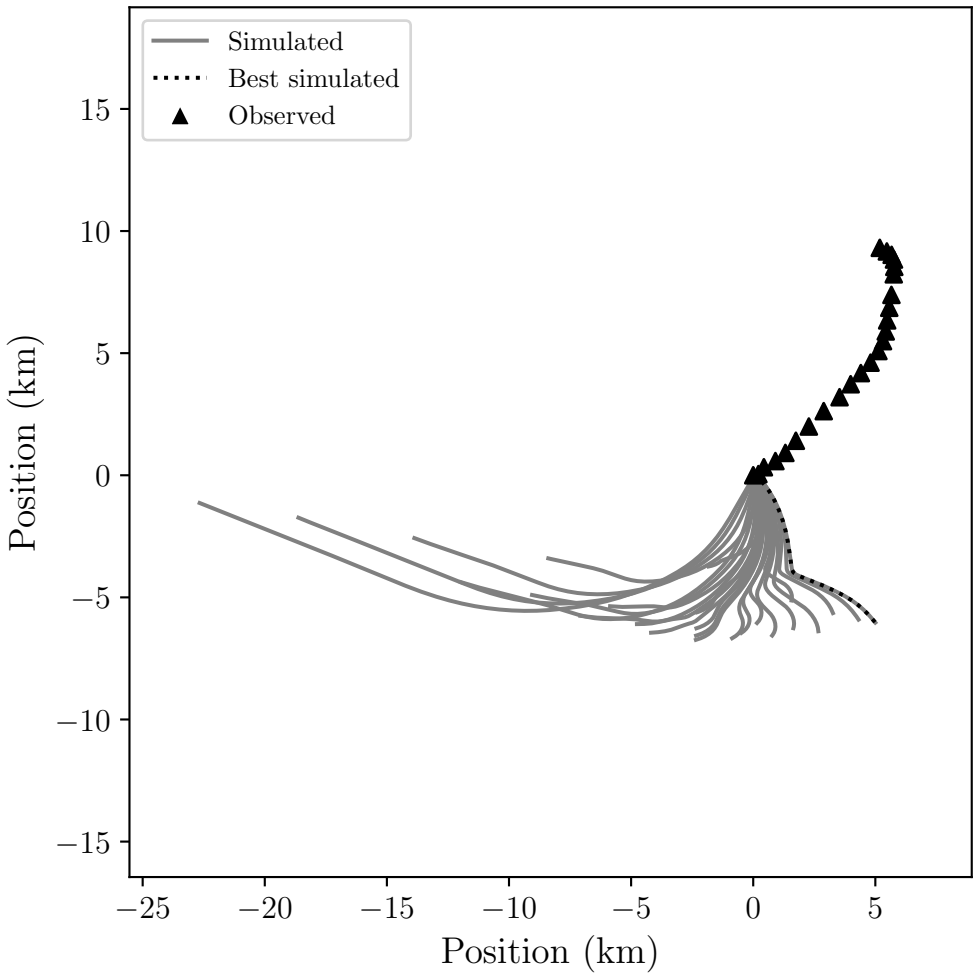

Figure 4.37: Iceberg drift simulations with various values of C_a and C_w. Each simulated run was evaluated for its agreement with the observed iceberg track based upon the root mean square error (RMSE) between the simulated run and the observed iceberg track.

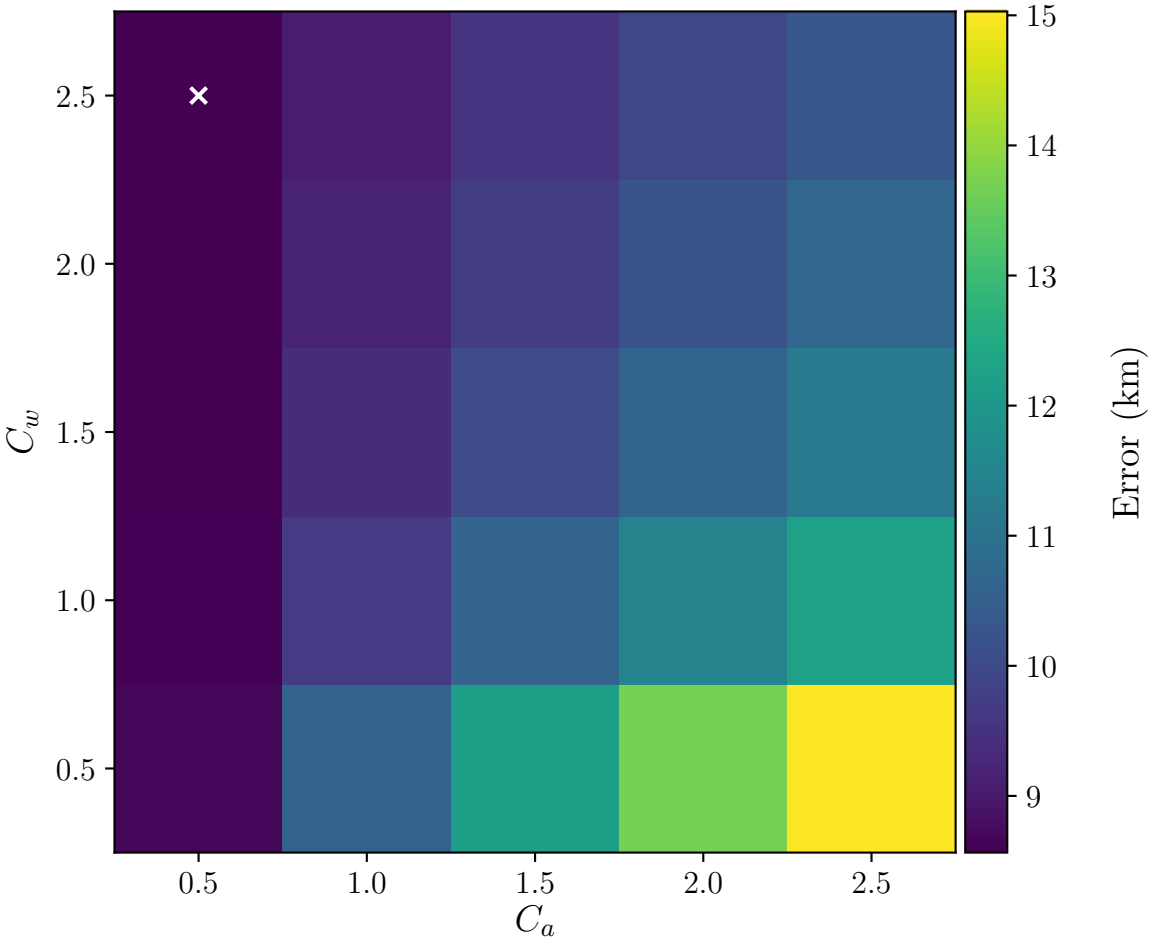

Figure 4.38: The error associated with the runs simulated with various values of C_a and C_w. The error is the root mean square error (RMSE) between the simulated track and the observed track (see Equation 4.2).

of this iceberg drift model to use the ECMWF and NARR ocean and atmospheric models to predict the path of an iceberg accurately.

If we then compare these results to their deterministic counterpart, we find that again we cannot encapsulate the observed drift track with any realistic values of C_a and C_w; however, the values found do correspond to a lower RMSE than in the ensemble approach (as seen in Figures 4.41 and 4.38).

Here we can see that the values of C_a and C_w that correspond to the lowest RMSE are 1.0 and 0.5, respectively, and the lowest RMSE is approximately 6.5 km. Notice, too, that only one of the drag coefficients, C_w, is at the boundary.

The probability map for this choice of parameters (seen in Figure 4.40), on the other hand, does not produce results that are much better. Again, almost all of the observed iceberg's location points lie in the zero probability region. This is just one example of a case where the forecast for an iceberg, whether done with a deterministic or ensemble approach, produce very inaccurate results. There are, of course, many factors that could have led to the bad forecast. One such factor could be a temporal offset between the model and actual metocean conditions. Referring back to Figure 4.40, one can see that the iceberg's forecast does begin to shift in the correct direction (towards the Northeast) at approximately mid-way through the forecast. This, likely, was due to a shift in the metocean conditions. If this shift occurred further back in time (towards the start of the forecast), the accuracy of the forecast may have improved dramatically. This emphasizes the need for accurate metocean data when making iceberg drift forecasts. Additionally, it would be beneficial to add further research to this work that would study various initial conditions and how they affect the accuracy of the forecast.

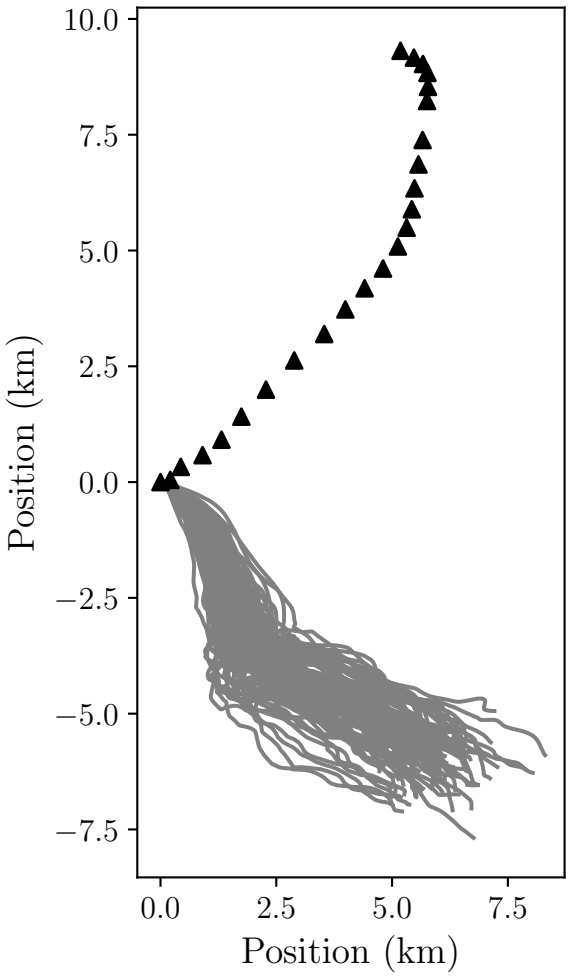

Figure 4.39: Ensemble of simulations performed by perturbing winds and currents by sampling from their determined distributions.

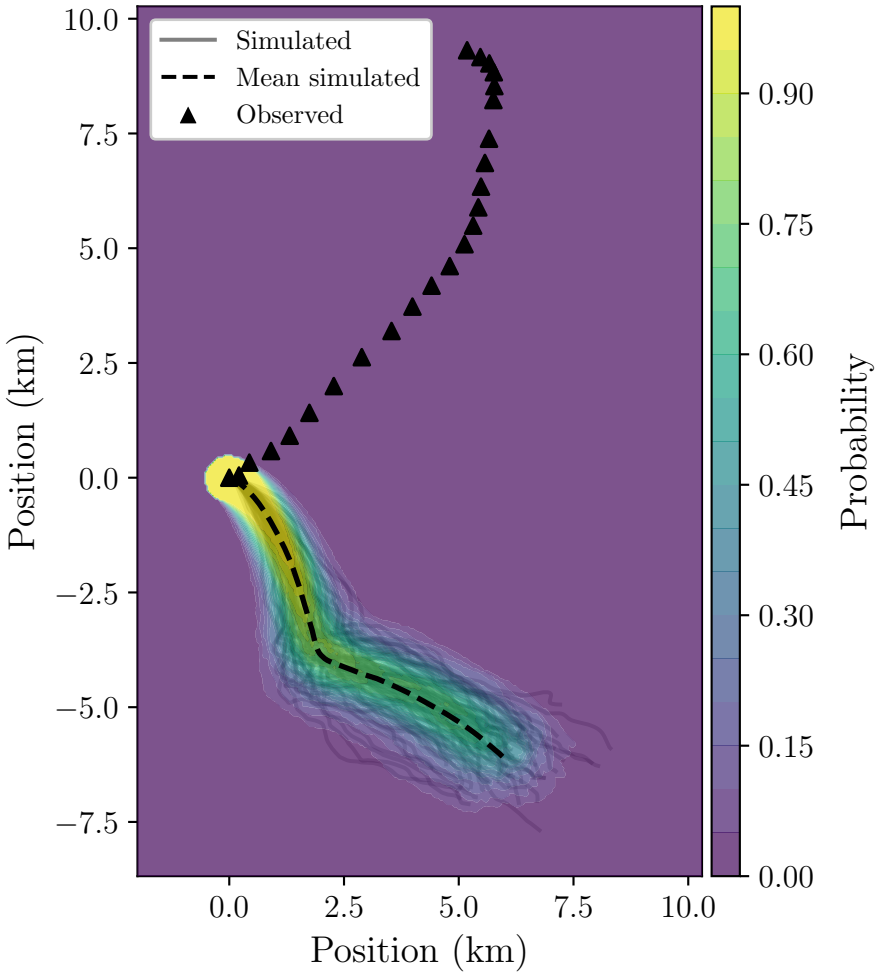

Figure 4.40: Probability of finding an iceberg which contained beacon 505190 deployed during the Statoil-ArcticNet research expedition of 2015 at any given location during the time span of the period between April 23rd 23:59:26 and 25th 00:58:13, 2015 based on the results of an ensemble drift prediction (with a radius set to 0.5 km).

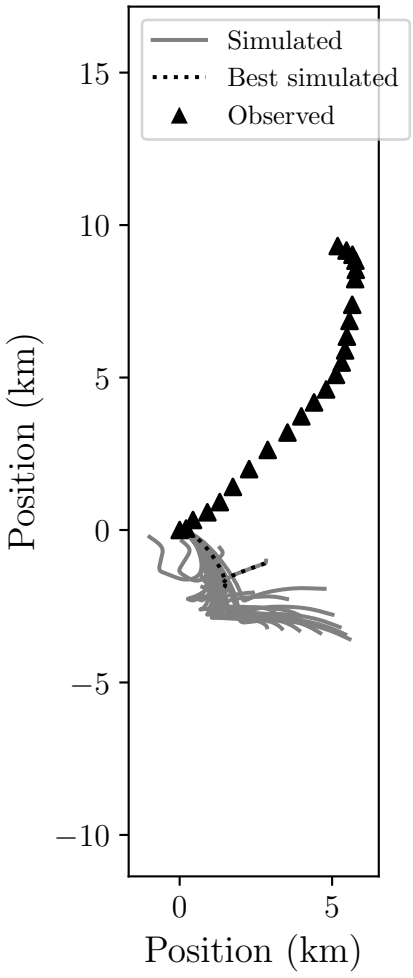

Figure 4.41: Iceberg drift simulations with various values of C_a and C_w and the means of the current and wind correction distributions added to the current and wind velocities; respectively. Each simulated run was evaluated for its agreement with the observed iceberg track based upon the root mean square error (RMSE) between the simulated run and the observed iceberg track.

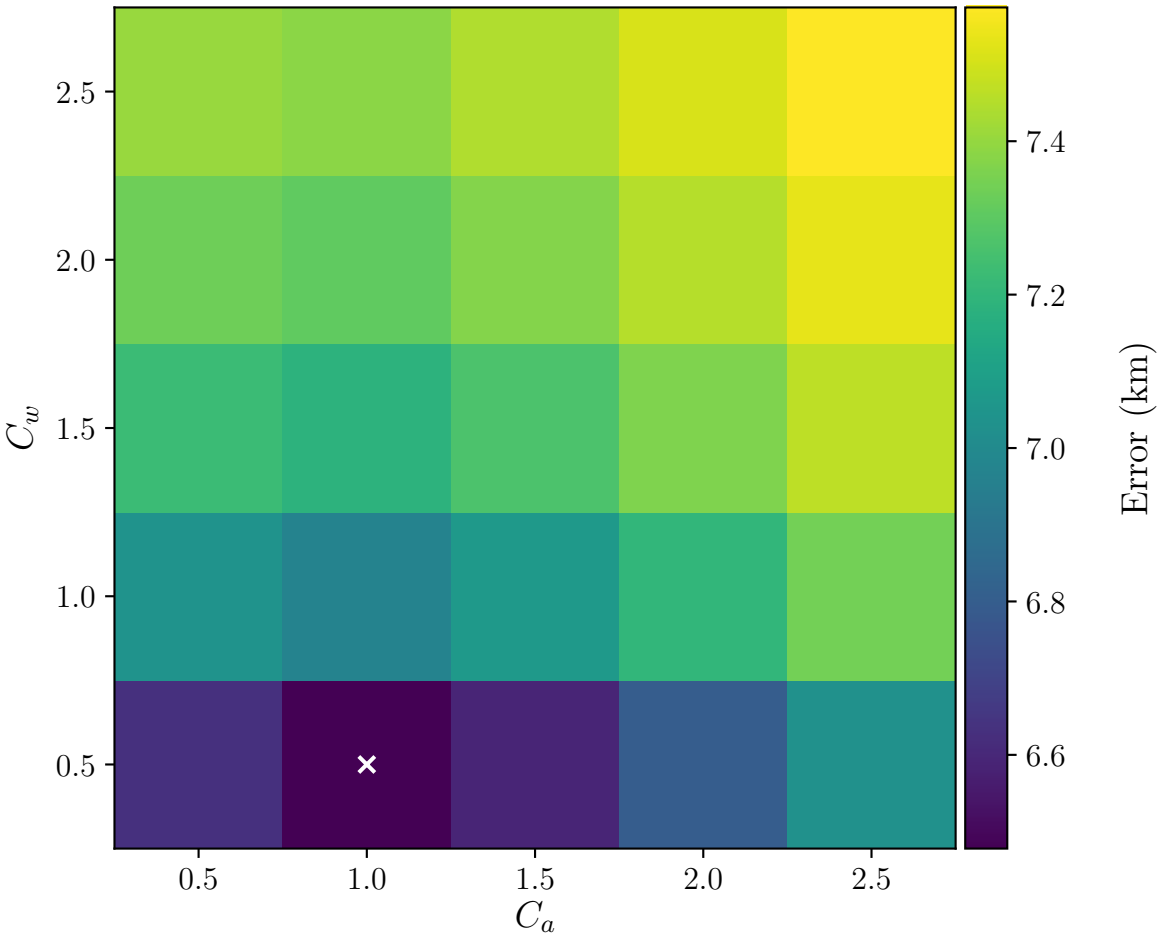

Figure 4.42: The error associated with the runs simulated with various values of C_a and C_w. The error is the root mean square error (RMSE) between the simulated track and the observed track (see Equation 4.2).

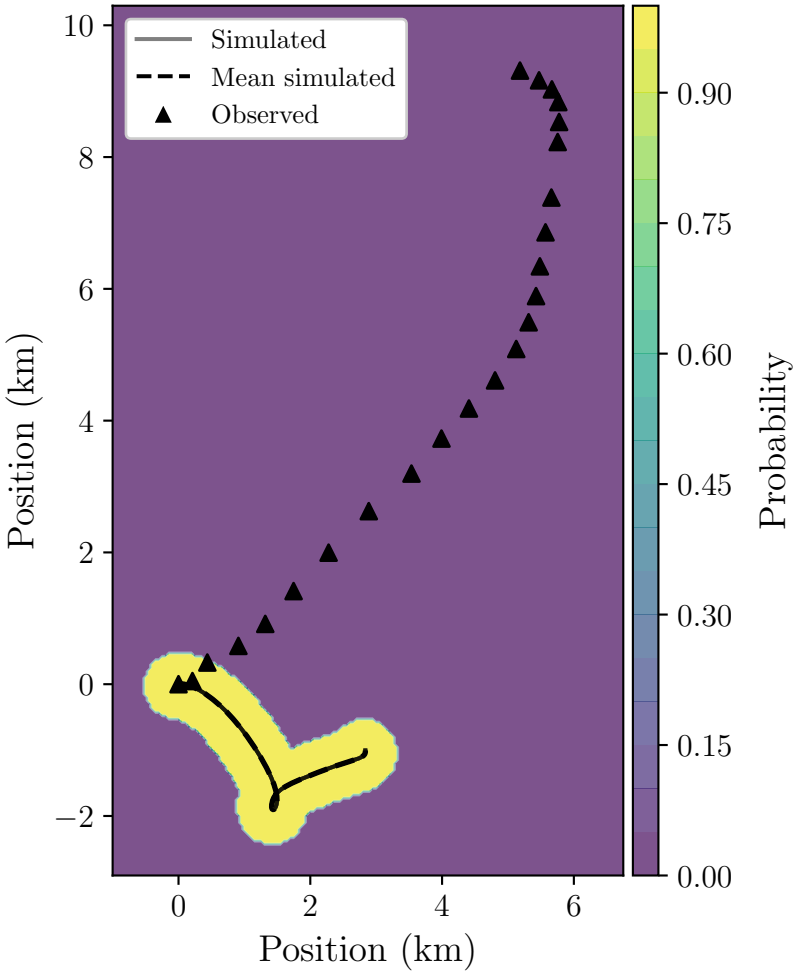

Figure 4.43: Probability of finding the iceberg which contained beacon 505190 deployed during the Statoil-ArcticNet research expedition of 2015 at any given location during the time span of the period between April 23rd 23:59:26 and 25th 00:58:13, 2015 based on the results of a single deterministic drift prediction (with a radius set to 0.5 km).

Chapter 5

Discussion

5.1 Summary

The results from using ensemble forecasting to predict the iceberg drift tracks from the Statoil-ArcticNet research expedition of 2015 showed that, although the ensemble technique can provide more information to those interpreting the results, the predictions vary greatly in terms of accuracy. In particular, the example that simulates the drift of the iceberg with beacon 906790 (henceforth known as the *good case*) encapsulated all of the observed iceberg location points within its spread, whereas the example that simulates the drift of the iceberg with beacon 505190 (henceforth known as the *bad case*) encapsulated only the first couple of points. This raises the question of why one such case can perform so well and the other so poorly?

When comparing the wind velocity data between the good and bad cases, it is seen that the wind speed varies more greatly in the bad case (0 – 8 m/s versus 5 – 7 m/s) and that there is a similar degree of variation in the direction (roughly the

90° between Southerly and Easterly versus roughly the 90° between Northeasterly and Southeasterly). In the context of wind speed for this region at this time of year, wind speeds between around 4 and 8 m/s would be considered average (see Figure 2.7). This means that the wind speeds in the good case can be considered average and those in the bad case would be low to average.

When comparing the current velocity data between the good and bad cases, it is seen that the current speed varies much more greatly in the bad case (0 – 0.3 m/s versus 0.1 – 0.2 m/s) and, likewise, the current direction varies much more in the bad case as well (roughly all 360° versus roughly the 90° between Northwestward and Northeastward). In the context of current speed for this region at this time of year, current speeds between around 0.2 and 0.4 m/s would be considered average (see Figure 2.5). This means that the current speeds in both cases would be considered low to average. The major difference between the current fields of the good and bad cases is definitely in the variation of the direction of the current velocity vectors, otherwise known as the divergence.

5.2 Implications

The question of whether or not using an ensemble approach (by perturbing the wind and current velocities using distributions of corrections) is of better use to those looking to make informed decisions that rely upon where an iceberg is predicted to go is still a matter of debate. On one hand, if iceberg drift predictions using both the ensemble and deterministic approaches were always reasonably accurate in regards to the actual iceberg trajectory, the ensemble approach would be better in the sense

that one could make decisions based upon probabilities within the range of 0 and 1 rather than just the extreme probability of values of 0 or 1 with a deterministic approach. On the other hand, if drift predictions are inaccurate any more than a fraction of the time they are used, decision-makers cannot possibly place all their faith in their results — especially, when the worst-case scenario for sea-faring vessels and oil platforms includes loss of human life.

5.3 Comparison to other studies

Although the practice of ensemble forecasting is popular in meteorology, there are very few published works in the field of iceberg drift forecasting. One such work, however, involves using a Monte Carlo approach to sample the parameter spaces of many unknown inputs into a drift model during simulation (Allison et al., 2014). In this study, the researchers ran Monte Carlo simulations with a range of variations for iceberg properties, driving forces, and initial conditions within the 95% confidence level of the parameter's value. Specifically, these parameters were: iceberg length and added mass, wind direction, speed, and drag coefficient, current direction, speed, and drag coefficient, wave height, stress coefficient, period, and direction, swell height, stress coefficient, period, and direction, initial position, speed, and direction. Aside from the fact that they perturbed many more parameters, this approach is similar to the one we employed; however, the ocean current and wind velocities they used were sampled from distributions that were created from the climate perspective of taking the current velocities around a specific location at a specific time of year over many years. This often leads to a very large ensemble spread which was motivation for our

approach of using observed measurements that were nearby, in both time and space, to the iceberg.

Another study which looked at icebergs from the same research expedition used in our work, and which uses an approach involving the addition of corrections to velocity data, was that of Andersson et al. (2016). This approach involves adding an artificial current, which the authors call an *ancillary current*, to the current depicted by an ocean model in order to change its direction and/or speed in favor of following an iceberg's trajectory more accurately. Specifically, by using this ancillary current, they modify the water drag force from

$$\mathbf{F_c} = \frac{1}{2}\rho_c C_w \sum_k A_c(k)|\mathbf{V_c}(k) - \mathbf{V_i}|(\mathbf{V_c}(k) - \mathbf{V_i}) \tag{5.1}$$

to

$$\mathbf{F_c} = \frac{1}{2}\rho_c A_c C_w|((\mathbf{V_{mc}} + \mathbf{V_c^*}) - \mathbf{V_i})|((\mathbf{V_{mc}} - \mathbf{V_c}) - \mathbf{V_i}) \tag{5.2}$$

where $\mathbf{V_{mc}}$ is the mean current in the water column over the iceberg keel and $\mathbf{V_c^*}$ is the velocity of the artificial current. When running simulations using this approach, their results showed slight improvement in the accuracy of their drift predictions. The problem with this is that the ancillary current is not known prior to the start of the simulation; rather, it is estimated as new measurements are received. This is where we hope our approach could benefit, since the distributions of corrections for the ocean current and wind velocities can be found prior to the start of simulation given that there are enough observational measurements from nearby regions.

Bibliography

K. Allison, G. Crocker, H. Tran, and T. Carrieres. An ensemble forecast model of iceberg drift. *Cold Regions Science and Technology*, 2014.

Amundsen Science Data Collection. AVOS meteorological data collected by the CCGS Amundsen in the Canadian Arctic. Amundsen Science, Québec, Canada. Processed data. Archived at www.polardata.ca, Canadian Cryospheric Information Network (CCIN), Waterloo, Canada. 2018. doi: https://doi.org/10.5884/12518.

L. E. Andersson, F. Scibilia, and L. Imsland. An estimation-forecast set-up for iceberg drift prediction. *Cold Regions Science and Technology*, 131:88–107, 2016.

E. Banke and S. Smith. Measurements of towing drag on small icebergs. In *Ocean '74 - IEEE International Conference on Engineering in the Ocean Environment*, pages 130–132, 1974.

A. Bentamy. Product user manual for wind product, version 1.3 WIND_GLO_WIND_L4_NRT_OBSERVATIONS_012_004. Technical report, EU Copernicus Marine Service, 2017. URL `http://marine.copernicus.eu/documents/PUM/CMEMS-WIND-PUM-012-004.pdf`.

G. Z. Brown. *Sun, wind & light architectural design strategies*. John Wiley & Sons, 2nd edition, 2001.

B. Cushman-Roisin. *Introduction to geophysical fluid dynamics: physical and numerical aspects*. International geophysics series; v. 101. Academic Press, 2nd edition, 2011.

D. Diemand. Icebergs. In J. H. Steele, editor, *Encyclopedia of Ocean Sciences*, pages 181 – 190. Academic Press, 2nd edition, 2001.

Environment Canada, Meteorological Service of Canada. *MANICE: Manual of Standard Procedures for Observing and Reporting Ice Conditions*, revised ninth edition, 2005. URL `https://www.canada.ca/en/environment-climate-change/services/weather-manuals-documentation`. Accessed: 2018-02-20.

R. E. Ettle. Statistical analysis of observed iceberg drift. *Arctic*, 27(2):121–127, 1974.

E. Hairer. *Solving ordinary differential equations*. Springer series in computational mathematics. Springer-Verlag, 1987.

International Ice Patrol (IIP). Iceberg sightings database, version 1, 1995, updated 2018. URL `https://doi.org/10.7265/N56Q1V5R`. Accessed: 2018-01-20.

G. L. Johnson and P. M. Moretti. Wind energy systems. *Journal of Solar Energy Engineering*, 1985.

F. Mauviel. Iceberg dynamical modelling. *Annals of Glaciology*, 1:123–127, 1980.

F. Mesinger. North American Regional Reanalysis: A long-term, consistent, high-resolution climate dataset for the north american domain, as a major improvement

upon the earlier global reanalysis datasets in both resolution and accuracy. Technical report, 2004.

L. Nouel. Quality information document for global sea physical analysis and forecasting product GLOBAL_ANALYSIS_FORECAST_PHY_001_024. Technical Report 2.0, EU Copernicus Marine Service, 2016. URL http://marine.copernicus.eu/documents/PUM/CMEMS-GLO-PUM-001-024.pdf.

Polar Data Catalogue. Aerial-photo and LiDAR iceberg surveys during the 2015 Joint Statoil/ArcticNet Cruise, Newfoundland and Labrador, Canada. 2015.

P. Rudkin. Comprehensive iceberg management database report 2005 update. Technical report, National Research Council of Canada (NRC) and Panel on Energy Research and Development, 2005.

L. D. Talley, G. L. Pickard, W. J. Emery, and J. H. Swift. Chapter 7 - Dynamical processes for descriptive ocean circulation. In L. D. Talley, G. L. Pickard, W. J. Emery, and J. H. Swift, editors, *Descriptive Physical Oceanography (Sixth Edition)*, pages 187 – 221. Academic Press, 2011.

I. D. Turnbull, N. Fournier, M. Stolwijk, T. Fosnaes, and D. McGonigal. Operational iceberg drift forecasting in Northwest Greenland. *Cold Regions Science and Technology*, 110:1 – 18, 2015.

G. K. Vallis. *Atmospheric and oceanic fluid dynamics : fundamentals and large-scale circulation*. Cambridge University Press, 2006.

T. J. W. Wagner, R. W. Dell, and I. Eisenman. An analytical model of iceberg drift. *Journal of Physical Oceanography*, 47(7):1605–1616, 2017.

V. Warren, J. Pennell, and D. Grover. Enquiry report: Ice incursion incident SeaRose FPSO. Technical report, C-NLOPB, 2018.